Contents lists available at ScienceDirect

European Journal of Medicinal Chemistry

Research paper

Structure-based design of multitargeting ChEs-MAO B inhibitors based on phenyl ring bioisosteres: AChE/BChE selectivity switch and drug-like characterization

Gabriella La Spada [a,1], Daniela Valeria Miniero [b,1], Mariagrazia Rullo [a,1], Marco Cipolloni [c], Pietro Delre [d], Carolina Colliva [c], Marco Colella [a], Francesco Leonetti [a], Grazia Maria Liuzzi [b], Giuseppe Felice Mangiatordi [d], Nicola Giacchè [c], Leonardo Pisani [a,*]

[a] Dept. of Pharmacy-Pharmaceutical Sciences, University of Bari Aldo Moro, via E. Orabona 4, 70125, Bari, Italy
[b] Dept. of Biosciences, Biotechnologies and Environment, University of Bari Aldo Moro, Via E. Orabona 4, 70125, Bari, Italy
[c] Tes Pharma s.r.l., via Palmiro Togliatti 20, 06073, Corciano, PG, Italy
[d] CNR, Institute of Crystallography, 70126, Bari, Italy

ARTICLE INFO

ABSTRACT

A structure-based drug design approach was focused on incorporating phenyl ring heterocyclic bioisosteres into coumarin derivative 1, previously reported as potent dual AChE-MAO B inhibitor, with the aim of improving drug-like features. Structure-activity relationships highlighted that bioisosteric rings were tolerated by hMAO B enzymatic cleft more than hAChE. Interestingly, linker homologation at the basic nitrogen enabled selectivity to switch from hAChE to hBChE. In the present work, we identified thiophene-based isosteres 7 and 15 as dual AChE-MAO B (IC$_{50}$ = 261 and 15 nM, respectively) and BChE-MAO B (IC$_{50}$ = 375 and 20 nM, respectively) inhibitors, respectively. Both 7 and 15 were moderately water-soluble and membrane-permeant agents by passive diffusion (PAMPA-HDM). Moreover, they were able to counteract oxidative damage induced by both H$_2$O$_2$ and 6-OHDA in SH-SY5Y cells and predicted to penetrate into CNS in a cell-based model mimicking blood-brain barrier. Molecular dynamics (MD) simulations shed light on key differences in AChE and BChE recognition processes promoted by the basic chain homologation from 7 to 15.

1. Introduction

Alzheimer's disease (AD) represents a devastating neurodegenerative disorder that progressively impairs daily-life activities by producing cognitive deficits, behavioural abnormalities, and memory loss [1]. AD accounts for 50–70% of total dementia cases and its prevalence increases with population ageing [2]. Difficulties for providing early diagnosis and the lack of truly disease-modifying options elicit a tremendous socioeconomic impact [3]. Actually, the histopathological evidence used to diagnose AD is represented by neuritic plaques composed by deposits of β-amyloid (Aβ) oligomers and intraneuronal aggregates of hyperphosphorylated tau protein, termed neurofibrillary tangles [4]. For several decades drug research in this field was inspired by the cholinergic hypothesis which led to the licensing of acetylcholinesterase (AChE) inhibitors that aim at counterbalancing acetylcholine (ACh)

depletion to relieve cognitive symptoms [5]. Thereafter, great efforts have been devoted to the so-called amyloid cascade hypothesis [6] until FDA approved two monoclonal antibodies directed at the brain clearance of Aβ, even if the amyloid contribution to cognitive decline remains controversial [7]. Indeed, both drugs slow down cognitive decline provided that they are administered at early stage of the disease. Moreover, uncomplete phase III data and severe life-threatening side-effects cast a shadow over these exciting results [8]. Unfortunately, even if many cellular players have been identified, the disease pathobiology of AD has not been fully elucidated. For all these reasons, a paradigm shift is needed for developing effective disease-modifying drugs. By focusing on the complex multifactorial nature of AD, researchers envisaged the so-called multitarget approach [9]. This strategy aims at identifying drug candidates able to control two (or more) cellular processes involved in the onset and/or the progression of the disease, termed

multitarget directed ligands (MTDLs) [10–13]. Within the complex scenario of neuronal aberrations affecting AD brains, the chemical frameworks of MTDLs are designed to address selected molecular targets that could work for additive and/or synergic effects. The cooperativity arising from multiple activity is thought to perform more effective therapeutic actions.

In the present manuscript, we report the rational design, the in vitro biological evaluation, and the drug-like characterization of a small collection of 2*H*-chromen-2-ones (coumarin) derivatives as multi-targeting inhibitors of cholinesterases (AChE and butyrylcholinesterase, BChE) and monoamine oxidases B (MAO B). AChE and BChE are serine hydrolases that terminate cholinergic impulse transmission through the hydrolysis of the neurotransmitter, ACh. According to the initial hypothesis about AD, clinical manifestations were ascribed to impaired cholinergic transmission, which led to market AChE inhibitors as ACh-sparing tools within central nervous system (CNS). Even if these drugs enable only symptomatic effect without blocking or retarding the neurodegenerative cascade, they still represent the cornerstone of Alzheimer's cure. BChE has more recently been regarded as a viable target to develop therapeutic options for AD. This isoenzyme is mainly localized within glial cells and its expression increases as disease progresses. In conditions of intense brain activity, BChE performs a compensatory activity in place of AChE [14], that could be substrate inhibited (at high concentration) or depleted by pathological conditions. Both ChEs co-localize with protein deposits [15,16], clinical AD hallmarks, and probably contribute to neurotoxicity. Moreover, BChE knockout mice showed diminished amyloid fibrils load [17]. Monoamine oxidases A and B (MAO A and B) are mitochondrial membrane-bound enzymes that represent challenging targets for MTDLs [10,18]. Both MAO isoforms are responsible for the catabolism of unhindered arylalkylamines, including xenobiotics and neurotransmitters. The oxidative deamination catalyzed by MAOs produces aldehyde by-products along with hydrogen peroxide. Therefore, MAOs have been considered a source of ROS at mitochondrial level, where they sustain the NLRP3 inflammasome pathway [19]. Increasing lines of evidence suggests that the early phase of AD has a prominent neuroinflammatory component, mainly involving microglia and astrocytes [20]. Reactive astrocytes release pro-inflammatory cytokines and overexpress MAO B [21]. On these

bases, the blockade of MAO B activity may contribute to mitigating the neuroinflammation process within AD brains. Moreover, the selective inhibition toward B isoform might be endorsed also to avoid side-effects like hypertensive crises triggered by halting MAO A activity in peripheral tissues (e.g., intestine) [22].

We have recently reported the earliest crystal structures of a dual AChE-MAO B inhibitor (compound **1**, Fig. 1), mutually bound to each target enzymes [23]. This coumarin inhibitor [24] was endowed with an outstanding in vitro inhibitory profile, whereas it suffered from critical drug-like issues mainly related to poor aqueous solubility. The X-ray crystallographic structures provided the structural template for a structure-based design strategy aimed at improving drug-likeness while maintaining dual-targeting features. Both directed and water-bridged hydrogen bonding interactions anchored the heterocyclic framework of **1** to the catalytic site of MAO B (in front of FAD cofactor) and to the peripheral anionic subsite (PAS) of AChE. A careful inspection of binding poses suggests that the terminal unsubstituted phenyl ring was surrounded by aromatic residues (4–5 Å centroid distance) engaging similar binding interactions with both active sites. Within AChE, the phenyl ring occupied the catalytic anionic subsite (CAS), stacking in front of the indole sidechain of W86 in a parallel-displaced arene-arene interaction. As for MAO B, the same ring was wedged into a hydrophobic region lined with aromatic residues. F118 (not shown), F103, and W119 were at contact distance with the phenyl ring, that was bound closer and almost orthogonal to F168 with a T-shape arrangement.

Based on the X-ray crystallographic snapshots of the dual hit **1**, in the present work we envisaged a structure-based approach focused on replacing the unsubstituted phenyl ring with less lipophilic hetero-aromatic fragments. Aiming at maintaining the dual-targeting profile while improving drug-likeness (in particular, aqueous solubility), some 5- and 6-membered heterocyclic rings were enrolled as bioisosteres of the phenyl ring to mimic the stacking interactions and improving compounds' polarity. During iterative hit- and lead-refinement in medicinal chemistry programs, the bioisosteric replacement of phenyl rings, by far the most popular scaffold in small molecules therapeutics, has been a common practice to improve potency and overcome physicochemical issues detrimental to ADME profile [25]. To this scope, both 5- and 6-termed cycles, containing one or two heteroatoms, were
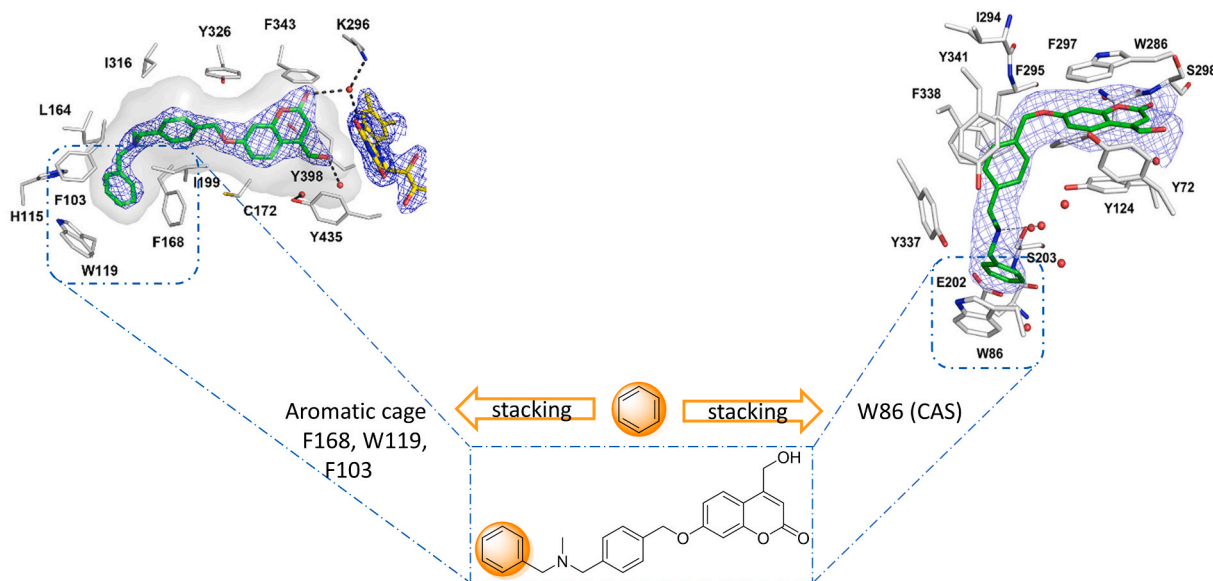

Fig. 1. Structure-based drug design strategy. X-ray crystallographic binding poses of hit compound **1** are shown in complex with human MAO B (PDB entry 7P4F, left) and mouse AChE (PDB entry 7QAK, right). Dashed frames highlight the binding regions of the terminal phenyl ring. Adapted from [F. Ekström, A. Gottinger, N. Forsgren, M. Catto, L.G. Iacovino, L. Pisani, C. Binda, Dual Reversible Coumarin Inhibitors Mutually Bound to Monoamine Oxidase B and Acetylcholinesterase Crystal Structures, ACS Med. Chem. Lett. 13 (2022) 499–506]. Copyright © 2022 The Authors. Published by American Chemical Society. This publication is licensed under CC-BY 4.0. To view a copy of this license, visit http://creativecommons.org/licenses/by/4.0/.

installed and their effect over in vitro inhibitory activities was determined toward target enzymes (*h*AChE, *h*BChE, *h*MAO A/B) along with early drug-like parameters, including aqueous solubility at physiological pH, chromatographic hydrophobicity index (CHI), and permeability through PAMPA-HDM (parallel artificial membrane permeation assay on hexadecane artificial membrane) method. The most active drug-like inhibitors were advanced toward the evaluation of metabolic stability in mouse microsomes, the ability to protect neuroblastoma cell lines from oxidative stress induced by two pro-oxidant insult, 6-hydroxydopamine (6-OHDA) and H_2O_2, and the assessment of blood-brain barrier (BBB) permeability through a cellular model.

2. Chemistry

The synthesis of final compounds **5–16** is illustrated in Scheme 1. Commercially available heterocyclic aldehydes were converted into the corresponding *N*-methyl(heteroaryl)methanamines **2a-i** through a reductive amination protocol employing methylamine (from 33 wt. % solution in absolute ethanol or hydrochloride salt, pre-treated with K_2CO_3) and $NaBH_4$ as reducing agent. *N*-Methyl-2-(pyridin-3-yl)ethan-1-amine (**2j**) was commercially available. Appropriate amine **2a-j** was then reacted with bromide **4a** [18] under nucleophilic substitution conditions to furnish coumarins **5–13, 16**. A different synthetic pathway was followed to prepare derivatives **14–15** bearing an homologated linker. Appel reaction, in the presence of PPh_3 and CBr_4, promoted the bromination of commercially available 2- or 3-thiopheneethanol to afford **3a-b**. Intermediate bromides **3a-b** were then reacted with amine **4b** [18], in turn obtained from bromide **4a** and methylamine in THF, thus yielding compounds **14–15**.
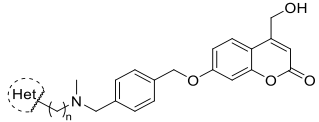
3. Results and discussion

3.1. Structure-activity relationships (SAR)

Bioisosteres **5–16** were screened in vitro as inhibitors of AChE, BChE, MAO A and B from human source by applying well-established protocols [26,27]. All inhibitory data are reported in Table 1, whereas bar graph in Fig. 2 has been used to focus the attention of the readers over the main targets (AChE, BChE, MAO B) discussed in SAR analysis in comparison with compound **1**. For the sake of clarity, MAO A/B selectivity was considered a crucial goal to avoid safety issues and was expressed as $SI_{MAO\ B}$ (Selectivity Index toward MAO B = IC_{50} MAO A/IC_{50} MAO B). On the other side the activity toward AChE or BChE could be equally beneficial against AD, since both isoenzymes are thought to play different and crucial roles depending on disease stage. Similarly, SI_{BChE} was calculated as AChE/BChE IC_{50} ratio.

Table 1

*In vitro* inhibition data toward *h*ChEs and *h*MAOs for compounds **1, 5–16**.

cmpd	Het	n	IC_{50} (μM) or % inhibition at 10 μM[a]			
			*h*AChE[b]	*h*BChE[c]	*h*MAO A[d]	*h*MAO B[d]
1	phenyl	1	0.120 ± 0.011	9.31 ± 0.72	15.2 ± 2.4	0.0102 ± 0.0021
5	thiophen-2-yl	1	0.501 ± 0.070	6.71 ± 0.03	45 ± 3 %	0.0360 ± 0.0071
6	furan-2-yl	1	0.832 ± 0.053	8.27 ± 0.04	5.16 ± 1.65	0.0175 ± 0.0035
7	thiophen-3-yl	1	0.261 ± 0.071	6.73 ± 0.23	42 ± 2 %	0.0153 ± 0.0022
8	imidazole-2-yl	1	1.32 ± 0.21	n.i.[e]	30 ± 4 %	0.0224 ± 0.0053
9	thiazol-2-yl	1	6.56 ± 0.39	n.i.[e]	48 ± 1 %	0.122 ± 0.014
10	thiazol-4-yl	1	1.78 ± 0.86	40 ± 2 %	31 ± 2 %	0.0195 ± 0.0008
11	pyridin-3-yl	1	0.985 ± 0.057	n.i.[e]	36 ± 6 %	0.0210 ± 0.0051
12	pyridin-4-yl	1	1.88 ± 0.11	n.i.[e]	2.47 ± 0.48	0.0524 ± 0.0041
13	pyrimidin-5-yl	1	4.06 ± 0.06	n.i.[e]	32 ± 4 %	0.0392 ± 0.0009
14	thiophen-2-yl	2	6.62 ± 1.01	0.875 ± 0.092	3.94 ± 1.68	0.0193 ± 0.0005
15	thiophen-3-yl	2	3.17 ± 0.26	0.375 ± 0.025	1.24 ± 0.11	0.0199 ± 0.0020
16	pyridin-3-yl	2	10.6 ± 2.8	0.620 ± 0.028	15.0 ± 4.3	0.177 ± 0.012
donepezil			0.0168 ± 0.0047	4.61 ± 0.33		
safinamide						0.0366 ± 0.0008
tacrine			0.109 ± 0.016	0.0316 ± 0.0108		

[a] Values are the mean of three independent experiments ± SEM. [b] Human AChE. [c] Human BChE. [d] Human recombinant MAOs on Supersomes. [e] n.i. = no inhibition or inhibition lower than 5 % at 10 μM concentration.

At a glance, none of derivatives **5-13** exhibited superior AChE inhibition compared to the reference dual AChE-MAO B inhibitor **1**. All heterocyclic analogues bearing 5-membered rings with 2 heteroatoms
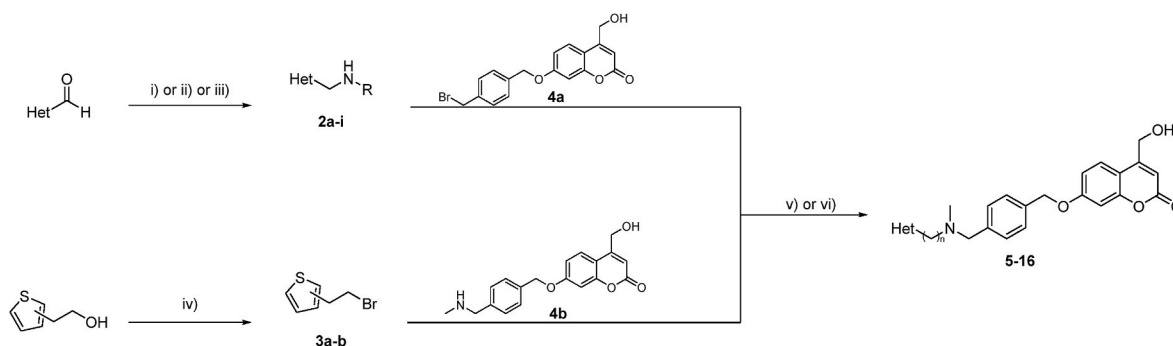
Scheme 1. Reagents and conditions: i) for **2a-c, 2i**: 1) CH_3NH_2·HCl, K_2CO_3, anhydrous methanol, room temperature, 1.5 h; 2) $NaBH_4$, anhydrous methanol, 0 °C to room temperature, 3 h; ii) for **2d, 2h**: 1) CH_3NH_2 (33 wt. % solution in absolute ethanol), anhydrous methanol, room temperature (for **2d**) or Δ (for **2h**), 0.5–2 h; 2) $NaBH_4$, anhydrous methanol, room temperature, 2–16 h; iii) for **2e-g**: 1) CH_3NH_2 (33 wt. % solution in absolute ethanol), molecular sieves (4 Å), Na_2SO_4 (for **2e**), anhydrous dichloromethane, room temperature, 16 h; 2) $NaBH_4$, abs. ethanol, room temperature, 3–16 h; iv) CBr_4, PPh_3, anhydrous dichloromethane, 0 °C to room temperature, 2 h; v) from **4a** and **2a-i** (or *N*-methyl-2-(pyridin-3-yl)ethan-1-amine, **2j**) for **5–13, 16**: TEA (for **5–7**) or K_2CO_3 (for **8–13, 16**), anhydrous acetone (for **5–13**) or anhydrous tetrahydrofuran (for **16**), room temperature, 2–24 h; vi) from **4b** and **3a-b** for **14, 15**: K_2CO_3, KI (cat), anhydrous acetonitrile, 70 °C, 7 h.
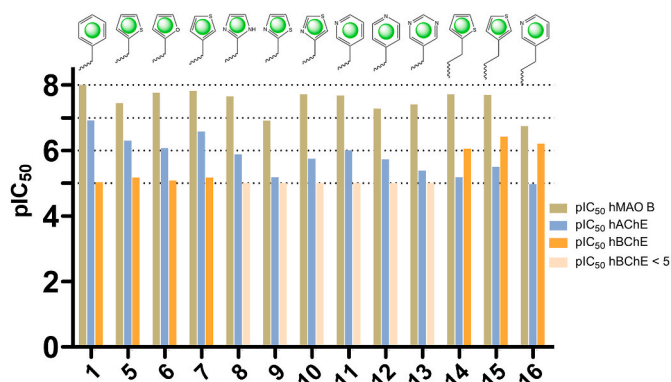
Fig. 2. Bar plot showing the inhibition data (pIC$_{50}$) for compounds **1**, **5**–**16** toward *h*MAO B, *h*AChE and *h*BChE. Semi-transparent orange bars for compounds **8**–**13** indicate pIC$_{50}$ values < 5 that were not exactly determined (at 10 μM: no inhibition or percentage of inhibition lower than 50%).

(**8**–**10**) or 6-membered rings (**11**–**13**) were active in the low micromolar range toward AChE (0.985 μM < IC$_{50}$ < 6.56 μM). Slightly better inhibition was allowed by 5-termed rings bearing one heteroatom (furan in **6**, thiophene in **5** and **7**) that showed submicromolar AChE inhibition while preferring the position 3 of the heterocycle for the branching substituent (**7** > **5**, **6**). No activities (**8**–**13**) or low-micromolar IC$_{50}$s (**5**–**7**), very close to reference **1**, were observed toward BChE.

Regarding the activity of **5**–**13** toward MAO B, most of the derivatives (**6**–**8**, **10**, **11**) showed IC$_{50}$ values significantly close to compound **1** as well as outstanding B/A selectivity. Thanks to the highest in vitro activity of the whole bioisosteric series toward both AChE (IC$_{50}$ = 0.261 μM) and MAO B (IC$_{50}$ = 0.0153 μM, SI$_{MAO B}$ > 667), compound **7** deserves attention as potent and selective dual AChE/MAO B inhibitor endowed with additional micromolar BChE inhibitory potency (IC$_{50}$ = 6.73 μM).

In this study, polar heterocycles were enrolled as phenyl ring bioisosteres to enhance the drug-like character of **1**. However, the electron-withdrawing character of the studied rings was not well-tolerated by target enzymes, resulting in widespread affinity drops. Moreover, these electron-withdrawing groups could, at least in part, counterbalance the polarity increase by lowering the pK_a of the basic nitrogen and reducing the ionized fraction at physiological pH. In order to sterilize this effect over compound's basicity, the linker homologation at one side of the basic nitrogen was investigated in compounds **14**–**16**. Surprisingly, this structural modification improved BChE selectivity over AChE, by reducing AChE inhibition ≈10-fold while shifting the potency toward BChE to the submicromolar range (IC$_{50}$ = 0.875 μM, 0.375 μM, and 0.620 μM for **14**, **15**, and **16**, respectively) whereas MAO B/A selectivity was decreased in comparison to shorter homologues (for **14**–**16**: 62 < SI$_{MAO B}$ < 204). Thus, linker homologation approach provided a straightforward strategy for reverting ChEs selectivity (8.5 < SI$_{BChE}$ < 17) and promoting BChE inhibition. Interestingly, MAO B inhibition for compounds **14**–**15** was not affected at a remarkable level by linker elongation (**14** > **5**, **15** ≈ **7**). Therefore, derivative **15** proved to be the most potent dual BChE/MAO B inhibitor within the present series, displaying the lowest IC$_{50}$ toward BChE (0.375 μM, SI$_{BChE}$ = 8.5) along with nanomolar potency toward MAO B (IC$_{50}$ = 0.0199 μM, SI$_{MAO B}$ = 62) and the inhibition of AChE at the low-micromolar level (IC$_{50}$ = 3.17 μM). An exception was represented by pyridyl derivative **16** displaying much lower activity than **1** toward MAO B (IC$_{50}$ = 0.177 μM) along with potent and selective BChE inhibition (IC$_{50}$ = 10.6 μM and 0.620 μM toward AChE and BChE, respectively; SI$_{BChE}$ = 17). As the consequence of poor MAO A inhibition, compound **16** was still endowed with a great MAO B/A selectivity (SI$_{MAO B}$ = 85) and a promising well-balanced multitarget profile as dual BChE/MAO B inhibitor showing potencies at the same order of magnitude (BChE IC$_{50}$ = 0.620 μM; MAO B IC$_{50}$ =

0.177 μM).

3.2. Drug-likeness evaluation

In many cases, the attrition rate of drug discovery programs depends on inadequate physicochemical properties that hamper hit progression in early animal studies or corrupt pharmacokinetic profile in more advanced (pre)clinical studies.

The aim of the present study was to improve the drug-like character of coumarin **1**, whose potent in vitro dual AChE-MAO B targeting profile was blurred by suboptimal aqueous solubility (14 μM, at pH 7.4) and critical hydrophobicity that impeded PAMPA permeation measurement. For this reason, the assessment of the drug-like character of novel bioisosteres was included in this study, encompassing the measurements of kinetic aqueous solubility (Table 3), hydrophobic character (Table 3), membrane permeability (Table 4), and the metabolic stability in mouse microsomes of selected prototypes (Table 4). Chemical shifts from ^{1}H NMR spectra listed in Table 2 demonstrated the more- or less-pronounced electron-withdrawing effect of bioisostere rings. Proton NMR signal attribution was also aided by 2D NOESY or HSQC spectra reported as supplementary data (Figs. S7–16 in Supplementary Material). In comparison to derivative **1**, nuclei at the C$_\alpha$-position of basic nitrogen showed chemical shifts distribution as function of both electron-withdrawing power (downfield: **5**–**13**) and relative distance (upfield: **14**–**16**) from heterocyclic bioisosteres. The thiophene ring substituted at position 2 (**5**) as well as 2- and 4-substitued thiazole (**9**–**10**) exerted the strongest deshielding impact.

As the consequence of this inductive effect, in most of the bioisosteres the basicity of *N*-sp^3 was mitigated to lower pK_a values than **1** (Table 2). Linker homologation in **14**–**16** attenuated the electron-withdrawing effect and enabled more basic functionalities. Chromatographic hydrophobicity index (CHI) [30] was used to assess compounds' hydrophobicity in three different buffered solution (pH 2.0, 7.4, 10.5) through a fast-gradient reversed-phase HPLC method (Table 3). Values obtained in alkaline buffer (pH 10.5) could be reliably attributed to the partitioning of the neutral forms (unionized). Basically, all compounds were less hydrophobic than **1**, with the thiophene-bearing isosteres **5**, **7**, **14**, and **15** showing the most apolar character. Since the gap between the CHI values at alkaline and physiological pH reflects differences in ionization states, compounds can be clustered into two subsets (**14**–**16** as stronger bases; **5**–**13** as weaker bases) and furthermore ranked according to basicity scale (**15** > **14**, **16**; **7** > **5**, **6**, **8**–**13**). Most of the predicted pK_as

Table 2

Effect of bioisosteric rings over pK_a and upfielding/downfielding of selected ^{1}H NMR chemical shifts for **5**–**16**.

cmpd	Het	pK_a			Chemical shifts (ppm)[d]	
		MoKa[a]	ACD[b]	Epik[c]	Het*CH$_2$*N	Het*CH$_2$CH$_2$*N
1	phenyl	7.89	7.78	7.87	3.50	
5	thiophen-2-yl	6.76	7.22	7.17	3.73	
6	furan-2-yl	7.82	7.38	7.22	3.55	
7	thiophen-3-yl	7.74	7.94	6.82	3.52	
8	imidazole-2-yl	8.10	5.01	6.83	3.55	
9	thiazol-2-yl	5.93	6.04	6.18	3.87	
10	thiazol-4-yl	7.59	6.44	6.95	3.69	
11	pyridin-3-yl	7.90	6.99	7.58	3.51	
12	pyridin-4-yl	6.86	6.71	7.49	3.51	
13	pyrimidin-5-yl	7.27	6.70	7.11	3.57	
14	thiophen-2-yl	8.40	8.25	8.19		2.62
15	thiophen-3-yl	8.14	8.43	8.13		2.59
16	pyridin-3-yl	8.20	8.06	8.22		2.58

[a] pK_a values of *N*-sp^3 centre estimated with MoKa version 3.2.2.
[b] pK_a values of *N*-sp^3 centre estimated with ACD/Labs version 6.09.
[c] pK_a values of *N*-sp^3 centre estimated with Epik 7 [28,29].
[d] Chemical shifts (ppm) of protons from CH$_2$-groups bound to *N*-sp^3. Data were taken from ^{1}H NMR spectra recorded at 400 MHz in DMSO-*d$_6$* (see Supplementary Material).

Table 3
Physicochemical properties of **1** and related bioisosteres **5–16**.

cmpd	Het	Solubility at pH 7.4 (μM)^a	CHI^b		
			pH 2.0	pH 7.4	pH 10.5
1	phenyl	14 ± 2	53.0	98.0	102.1
5	thiophen-2-yl	8 ± 1	50.4	96.5	98.0
6	furan-2-yl	40 ± 1	47.2	83.5	85.1
7	thiophen-3-yl	19 ± 1	50.7	90.3	95.0
8	imidazole-2-yl	33 ± 19	34.6	51.6	50.7
9	thiazol-2-yl	24 ± 1	42.7	76.7	76.1
10	thiazol-4-yl	81 ± 16	42.2	68.3	69.9
11	pyridin-3-yl	51 ± 3	32.9	70.6	70.9
12	pyridin-4-yl	45 ± 1	32.3	72.8	72.0
13	pyrimidin-5-yl	72 ± 2	35.9	62.6	61.4
14	thiophen-2-yl	19 ± 1	53.7	92.9	97.8
15	thiophen-3-yl	32 ± 1	54.3	85.5	95.2
16	pyridin-3-yl	115 ± 5	29.9	65.3	69.3

^{a} Kinetic solubility determined in PBS at pH 7.4 from duplicate analysis by UV–Vis spectrophotometry. Values are the mean ± SEM.

^{b} Chromatographic hydrophobicity index (CHI) determined through a fast-gradient reversed-phase HPLC method at three different pH values (2.0, 7.4, 10.5).

Table 4
Permeation data of **1**, **5–16** and metabolic stability in mouse microsomes of selected compounds (**1**, **7**, **15**, **16**).

cmpd	Het	PAMPA-HDM			microsomal stability (mouse)	
		logP_a (cm/s)^a	1-R_M^{b}	classification	$t_{1/2}$(min)^c	CL$_{int}$^{d}
1	phenyl	n.d.^{e}	–	–	31.7 ± 0.1	43.9 ± 0.1
5	thiophen-2-yl	n.d.^{e}	–	–		
6	furan-2-yl	−4.6 ± 0.1	–	moderate		
7	thiophen-3-yl	−4.2 ± 0.2	–	high	22.7 ± 3.9	61.2 ± 10.4
8	imidazole-2-yl	< −6.5	0.5	low		
9	thiazol-2-yl	−4.2 ± 0.1	–	high		
10	thiazol-4-yl	−4.6 ± 0.1	–	moderate		
11	pyridin-3-yl	−4.6 ± 0.1	–	moderate		
12	pyridin-4-yl	−4.4 ± 0.1	–	high		
13	pyrimidin-5-yl	−5.2 ± 0.1	–	low		
14	thiophen-2-yl	−4.0 ± 0.3	–	high		
15	thiophen-3-yl	−4.1 ± 0.3	–	high	13.5 ± 0.7	103 ± 5
16	pyridin-3-yl	−4.9 ± 0.1	–	moderate	5.97 ± 0.22	233 ± 9

^{a} Logarithm of apparent permeability in Parallel Artificial Membrane Permeation Assay (PAMPA) with a hexadecane artificial membrane (HDM). Values are the mean ± SD from duplicates by UV-Vis spectroscopy.

^{b} Membrane retention where R_M is the membrane retention factor.

^{c} Half-life in mouse microsomes expressed in minutes. Values are the mean ± SD from duplicates by LC-MS/MS analysis.

^{d} Intrinsic clearance expressed in μL/(min × mg) protein. Values are the mean ± SD from duplicates.

^{e} Not determined (low aqueous solubility).

in Table 2 are in full agreement with this hypothesis.

Aqueous solubility depends on different structural factors, including the presence of polar groups, basicity tuning, and crystal lattice energy, among others [31]. Kinetic solubility values obtained at pH 7.4 were reported in Table 3 and illustrated in Fig. 3. Except for 2-thienyl bioisostere **5** showing a solubility at pH = 7.4 even lower than **1**, the introduction of more polar heteroaromatic phenyl ring isosteres in compounds **6–13** resulted in increasing solubility, although less significantly than expected (Table 3). Therefore, all derivatives belonged to the range of drugs with moderate solubility (10 μM < $S_{7.4}$ < 100 μM). The negligible or moderate effect over aqueous solubility in this series could be partially ascribed to the unfavourable pK_a shift promoted by electron-withdrawing heterocycles opposing lower hydrophobic characters (i.e., lower CHI values). As a matter of fact, linker homologation (**14–16**) attenuated pK_a decrease and improved solubility (Fig. 3: **14** > **5**, **15** > **7**, **16** > **11**). Basicity tuning was also achieved by less powerful electron-withdrawing substitution patterns (larger windows between CHI$_{7.4}$ and CHI$_{10.5}$ values, upfield chemical shifts), then more favourable protonation degrees raised compound's solubility (**7** > **5**, **10** > **9**). Polarity increase allowed by nitrogen-containing 6-membered cycles (pyridine and pyrimidine), exhibiting among the lowest CHI scores along with thiazole **10**, enabled to improve aqueous solubility for bioisosteres **10–13** by at least 3-fold (Fig. 3). Noteworthy, dual BChE/MAO B targeting compound **16** ($S_{7.4}$ = 115 μM) could be classified as highly water-soluble molecule (solubility value higher than 100 μM), thanks to both polar character and basicity mitigation that returned an 8-fold improvement in comparison to **1** (see Table 2 and Fig. 3).

A PAMPA setup on hexadecane membrane (HDM) was used as an in vitro protocol to mimic cellular and gastrointestinal permeation, and to assess biomembrane permeation by passive diffusion. The data listed in Table 4 proved that bioisostere approach supported the permeation for the majority of compounds, resulting in moderate-to-high apparent permeability scores. Exceptions were returned by more polar pyrimidin-5-yl derivative **13** (low permeant) and imidazole **8**, whose membrane permeability was strongly affected by high membrane retention ($\approx$ 50%). As a possible explanation, polarity and hydrogen bonding features for **8** could induce an unfavourable desolvation effect upon partitioning with the hydrophobic matrix [32].

Since first-pass effect is a crucial event affecting oral bioavailability, the most promising in vitro multitarget inhibitors were further progressed to metabolic stability studies in mouse microsomes. Taking into account the above-mentioned drug-like features (solubility, permeability) and in vitro inhibitory potencies, compound **7** (highly permeant
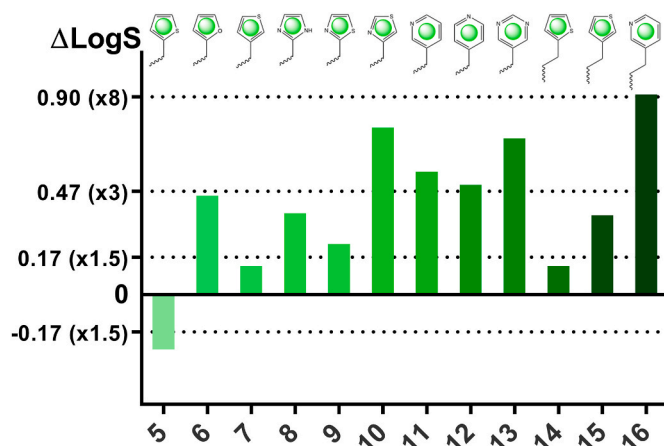

Fig. 3. Bar diagram showing the changes in aqueous solubility at pH 7.4 for **5–16** compared to **1**. The following equation was used: ΔLogS = LogS$_{7.4}$ (**1**) – LogS$_{7.4}$ (**compound**). The ticks of the positive Y-axis at 0.17, 0.47, and 0.70 indicate 1.5-fold, 3-fold and 8-fold solubility increase, respectively. The tick of the negative Y-axis at 0.17 indicates 1.5-fold solubility decrease.

and moderately water-soluble) and its homologue **15** were enrolled in this investigation as the most potent dual AChE-MAO B and BChE-MAO B inhibitor, respectively. Moreover, pyridine **16** was submitted to metabolic stability assessment thanks to its superior solubility outcome. As reported in Table 4, compound **7** can be considered the most metabolically stable bioisostere with a promising half-life equal to 22.7 min, even if lower than reference compound **1**. Higher clearance rates were measured for congener **15** as well as for **16**, where the pyridine ring can act as a metabolic hot-spot, thereby limiting in vivo exposure.

3.3. Cell-based assays: cytotoxicity, neuroprotection, and permeation studies

Thiophene-based isosteres **7** and **15** were chosen as prototypes of two different bioactivity profiles (AChE-MAO B and BChE-MAO B inhibition, respectively) and their cytotoxicity was evaluated in SH-SY5Y cell line, along with the most water-soluble compound **16**. As displayed by Fig. 4, isosteres **7** and **15** were quite safe compounds even at the highest concentration applied (100 μM), whereas the incubation with pyridine **16** decreased significantly the amount of viable cells starting from 50 μM to 100 μM.

Human neuroblastoma cells treated with 6-hydroxydopamine (6-OHDA) or hydrogen peroxide represent well-established cell-based models for neurodegeneration [33], that can be applied to evaluate the neuroprotective activity of novel compounds at a preliminary level before enrolling more complex disease models. Both insults are able to trigger oxidative stress conditions ultimately leading to neuronal death [34,35]. Compounds under study (**7**, **15**, or **16** at three different concentrations from 0.1 to 5 μM) were added to co-incubation experiments with the aim of investigating their ability to neutralize the neurotoxic effect of pro-oxidative insults [36] by measuring viable cells through [3-(4,5-dimethylthiazol-2-yl)-2,5-diphenyl tetrazolium bromide] (MTT) assay. Fig. 5A shows that, in particular, compounds **7** and **15** enabled a remarkable viability gain in SH-SY5Y cells insulted by 6-OHDA, even at the lowest concentrations applied (0.1–1 μM). Notably, nanomolar concentration of both bioisosteres returned neuroprotective activities comparable to donepezil, used as positive standard anti-AD drug. Derivative **16** was more effective than **7** and **15** against H_2O_2 (Fig. 5B)

within 0.1–1 μM range. At 5 μM, the cytoprotective effect of **16** (against both insults) and **15** (against 6-OHDA) was not significant, probably limited by inherent compounds' toxicity.

An in vitro BBB-mimicking model was built by co-culturing an endothelial cell line (mouse bEnd3 cells) together with an astrocyte cell line (DI-TNC1) [37] on a solid insert endowed with a pore-membrane (0.4 μm). The system integrity was guaranteed by the measurement of transendothelial electrical resistance (TEER) and the permeability of fluorescein isothiocyanate-dextran (FITC-D) as marker of paracellular transport. Preliminarily, the biocompatibility of both **7** and **15** upon incubation in these cultures was assessed from 1 to 100 μM concentration (Fig. S22 in Supplementary Material). As indicated in Table 5, compounds **7** and **15** could be considered BBB-permeant molecules that returned permeability values close to donepezil, chosen as standard CNS-active drug. Their ability to permeate the co-cultured monolayer was quite superior to FITC-D, that diffuses across biomembranes through paracellular pathways.

3.4. Computational studies

Molecular dynamics (MD) simulations were performed to elucidate the molecular determinants underlying the different binding affinities observed for thiophene-based bioisosteres **7** and **15** toward hAChE and hBChE (Table 1). Even though a quite simple structural modification was introduced, one methylene-unit homologation enabled to switch isoform selectivity remarkably. Indeed, **7** exhibited a strong preference for hAChE ($IC_{50} = 0.261$ μM) compared to hBChE ($IC_{50} = 6.73$ μM), whereas **15** displayed a reversed bioactivity profile favoring hBChE ($IC_{50} = 0.375$ μM) over hAChE ($IC_{50} = 3.17$ μM). Preliminarily, molecular docking simulations for both inhibitors within the binding sites of AChE and BChE enzymes were run. As for the protein templates, high-resolution crystal structure for *h*BChE (pdb code 7AWG [38]) in complex with a benzylamine derivative was employed. Regarding AChE, we recruited the X-ray crystallographic data of *mus musculus* AChE (*m*AChE) binary complex with **1** (pdb code 7QAK [23]) because of high sequence homology with human enzyme and the structural similarity between the cognate ligand compared to congeners **7** and **15**.

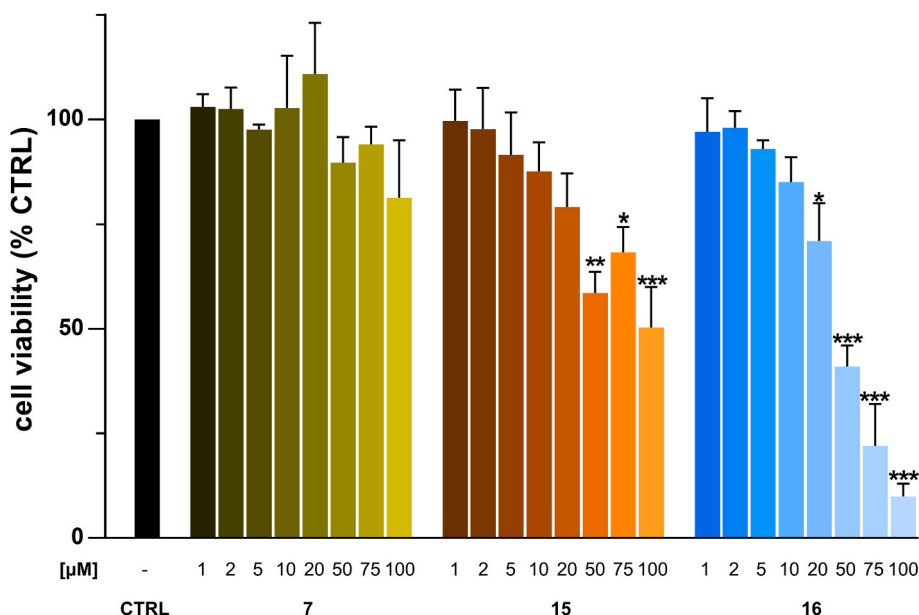Notably, the predicted binding modes (see Fig. S18 in Supplementary

Fig. 4. Cell viability of neuroblastoma SH-SY5Y cells in the presence of compounds **7**, **15**, and **16** (1–100 μM concentration range, 24 h incubation), as determined by MTT assay. Bars represent the mean ± SD of three independent experiments each performed in triplicates and referred to untreated control cells (CTRL, 100% value, in the absence of compounds). Statistical significance was calculated using one-way analysis of variance (ANOVA) followed by the Dunnett's multiple comparison test. Levels of significance referred to untreated cells: *p < 0.05, **p < 0.01, ***p < 0.001.
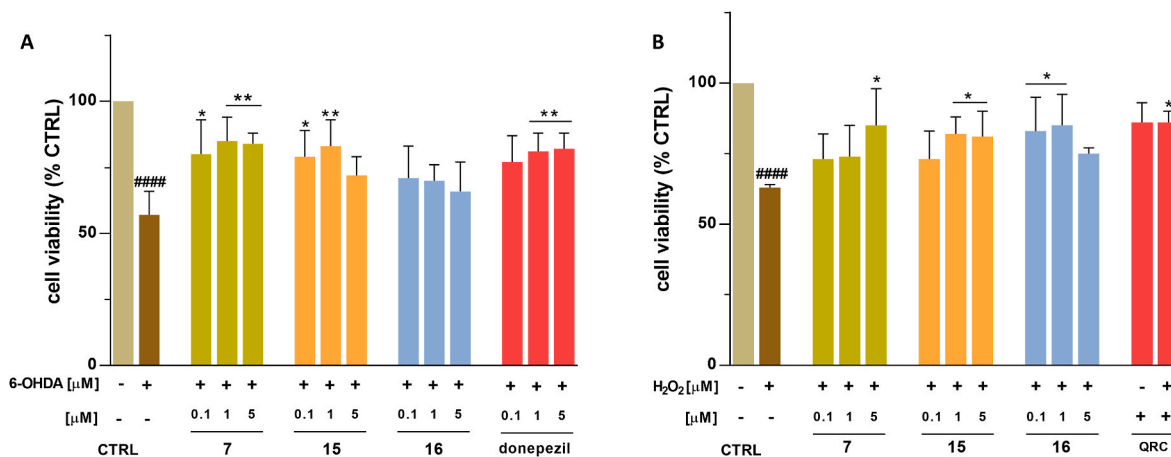
Fig. 5. Cytoprotective effect of compounds **7**, **15**, and **16** (0.1–5 μM concentrations range) co-incubated for 24 h with different oxidative insults (**A**: 6-hydroxydopamine, 200 μM; **B**: H$_2$O$_2$, 300 μM) on SH-SY5Y cell viability. Donepezil (0.1–5 μM, panel **A**) and quercetin (QRC, 30 μM, panel **B**) were used as positive controls. Results are expressed as % of cell viability measured through MTT test and are referred to untreated cells (CTRL, 100% values, without compounds). Bars represent the mean ± SD of three independent experiments, each performed in triplicates. Statistical significance was calculated using one-way analysis of variance (ANOVA) followed by Dunnett's multiple comparison test. Levels of significance referred to cells treated with insults alone: *p < 0.05, **p < 0.01. Levels of significance referred to untreated cells (control): ####p < 0.0001.

Table 5
BBB permeation data of derivatives **7** and **15**.

cmpd	Apparent permeability P_a (x 10^{-6} cm/s)[b]
FITC-D[a]	1.4 ± 0.2
donepezil	8.9 ± 0.1
7	8.0 ± 0.9
15	5.9 ± 0.6

[a] Fluorescein isothiocyanate-dextran (FITC-D).
[b] Apparent permeability across bEnd3/DI-TNC1 co-cultured on inserts with a diameter of 10.5 mm containing a track-etched poly(ethylene terephthalate) (PET) membrane (0.4 μm pores). Values are the mean ± SD from triplicates by fluorescence spectroscopy.

Material: top-scoring poses) closely resemble those observed for the cognate ligands and molecular recognition appears to be primarily driven by ionic interactions involving aspartate residues (D74 in *m*AChE, D70 in *h*BChE), hydrogen bonds, and π-π stacking. Computed docking scores closely match the in vitro experimental activities, demonstrating a more favourable binding profile for **7** within *m*AChE (−20.293 kcal/mol vs. −18.645 kcal/mol for **15**) and a preference for **15** toward *h*BChE (−11.527 kcal/mol vs. −10.899 kcal/mol for **7**).

Building upon these promising initial docking results, we employed the top-scored poses to conduct 150-ns-long MD simulations. The primary objective was to assess the stability of the predicted inhibitor-protein complexes (i.e., *m*AChE-**7**, *m*AChE-**15**, *h*BChE-**7** and *h*BChE-**15**) and identify key factors contributing to the selectivity switch. To evaluate protein stability during the simulations, we calculated the Root Mean Square Deviations (RMSD) of alpha-carbon atoms over time (Fig. S17 in Supplementary Material). This analysis indicated
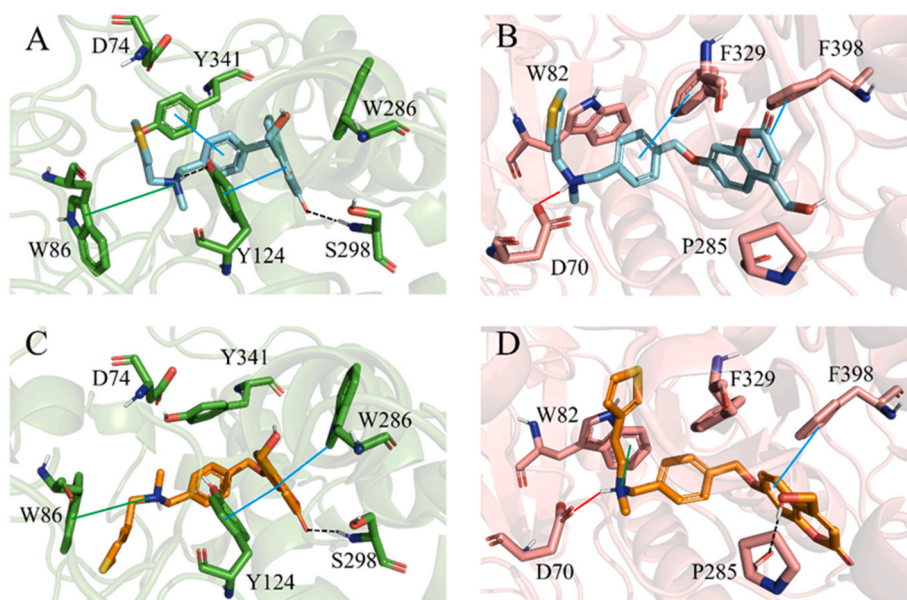

Fig. 6. Selected snapshots returned by the performed MD simulations: A) **7**-*m*AChE complex; B) **7**-*h*BChE complex; C) **15**-*m*AChE complex and D) **15**-*h*BChE complex. H-bonding, π-π, and cation-π interactions are itemized by a dotted black line, a cyan line, and a green line, respectively. For the sake of clarity, only polar hydrogen atoms are shown.

equilibration within 80 ns for all complexes. Subsequent analyses focused on the equilibrated portions of the generated trajectories, specifically the final 70 ns. Regarding the ligands, the obtained RMSD values supported the reliability of the adopted docking protocol, with values as low as 2.61 ± 0.06 Å (*m*AChE-**7**), 1.03 ± 0.33 Å (*m*AChE-**15**), 1.77 ± 0.10 Å (*h*BChE-**7**), and 1.63 ± 0.15 Å (*h*BChE-**15**). The binding poses of both inhibitors within AChE complexes were stabilized by binding contacts with the sidechains of S298, W86, and Y124 throughout the simulation. It is worth noting that derivative **7** adopted a different conformation positioning the thiophene moiety upwards during the simulations (Fig. 6A). On the other side, the rotational freedom of more flexible **15** (Fig. 6C) seemed to be somehow restricted to the point that the thiophene motif did not explore any other binding accommodations. The rearrangement experienced by **7** improves the inhibitor's stability within the enzymatic pocket, as highlighted by the root-mean-square-fluctuations (RMSFs) returned by the alkyl-thiophene moiety (0.2 Å vs. 0.4 Å for **7** and **15**, respectively). Probably, steric or entropic penalties prevented to shift and lock the thiophene ring of **15** in a more stable binding interactions as suggested by the higher RMSF. This could partially explain the lower affinity observed toward AChE upon the addition of a methylene group in the linker.

After a careful inspection of the postulated binding mode for **7** within *m*AChE, Y124 was predicted to play a pivotal role as it anchored the inhibitor by means of two interactions (hydrogen bond and π-π) for over 80% of the simulation time. Notably, there was also a highly stable cation-π interaction pointing toward W86 (occupancy of 93% for **7**, compared to 82% for **15**).

Regarding the MD simulations of **7** and **15** with *h*BChE (Fig. 6B and D), the binding poses differed mainly in the stability of the π-cation interaction directed to W82, close to the catalytic site (W86 in AChE). The much higher occupancy scored by **15** (≈ 70%) endorsed a greater stability for this binding contact compared to **7** (occupancy ≈ 23%). The higher flexibility (or the more pronounced basicity) allowed by the additional methylene group in **15** induced a slightly different orientation of the protonated chain positioning the nitrogen atom closer to the indole ring of W82 (Fig. S19 in Supplementary Material). Indeed, this binding mode was stabilized by a stronger interaction enhancing the inhibitory activity of **15** in comparison to **7** by ≈ 20-fold. These findings may elucidate the selectivity shift caused by linker elongation and further supported the well-established role of W86/W82 in AChE and BChE molecular recognition, recruiting substrates/inhibitors in both BChE [39] and AChE [40] through π-cation interactions as proved by mutagenesis experiments.

4. Conclusion

Aiming at improving the drug-likeness of a previously reported coumarin-based MTDL (**1**), molecular design was guided by a structure-based approach. Starting from the X-ray crystallographic poses of **1**, diverse heteroaromatic phenyl ring isosteres were recruited to mimic stacking interactions. SARs analysis on target enzymes highlighted that these heterocycles produced an activity decrease, which was more significant toward hAChE than hMAO B. Thus, most of the novel compounds displayed low nanomolar selective inhibition of hMAO B along with low micromolar to submicromolar IC_{50} toward hAChE. By homologating the linker at the basic nitrogen we scored an interesting ChEs selectivity switch, thus obtaining potent dual BChE/MAO B inhibitors. In particular compounds **7** and **15**, bearing a 3-substituted thiophene as phenyl ring bioisostere, were the most potent dual AChE-MAO B (IC_{50} = 261 and 15 nM, respectively) and BChE-MAO B (IC_{50} = 375 and 20 nM, respectively) inhibitors. Computational studies were conducted with the goal of elucidating the molecular determinants shifting ChEs isoform selectivity. The basic nitrogen atom in both **7** and **15** hooked the inhibitors to the indole ring of W86 residue in AChE. MD simulations hypothesized a conformational rearrangement yielding a more productive binding orientation of the thiophene core for **7**,

whereas a similar rotamer was forbidden for the more flexible derivative **15** due to steric shield and/or to unfavourable entropic factors in the enzymatic cavity of AChE. On the other hand, the higher flexibility degree and the increased basicity brought by ethyl-linker in **15** settled the protonated *N*-atom in closer contact with W82 within BChE, thus establishing a stronger and more stable cation-π interaction. With few exceptions, bioisosteric replacement enhanced aqueous solubility at physiological pH compared to **1** (at least by 1.5-fold) and returned favourable biomembrane permeation values in PAMPA-HDM experiments. Moreover, prototypes **7** and **15** proved to be able to counteract the toxic effect of pro-oxidants over SH-SY5Y lines in cell-based models of neuroprotection. Good metabolic stability in mouse microsomes and ability to permeate BBB in a co-culture in vitro model further endorsed the drug-like character of thiophene-containing **7** and **15** that deserve further attention as small molecular tools against neurodegenerative disorders like AD.

5. Experimental section

5.1. Chemistry. General methods

Starting materials, reagents, and analytical grade solvents were purchased from Sigma-Aldrich, Alfa-Aesar or Fluorochem (Europe). The purity of all the intermediates, checked by RP-HPLC, was always better than 95%. All the newly prepared and tested compounds showed purity higher than 95% (elemental analysis). Elemental analyses were performed on the EuroEA 3000 analyzer. The measured values for C, H, and N agreed to within ±0.40% of the theoretical values. Column chromatography was performed using Merck silica gel 60 (0.063–0.200 mm, 70–230 mesh). Flash chromatographic separations were performed on Biotage SP1 purification system using flash cartridges prepacked with KP-Sil 32–63 μm, 60 Å silica. All reactions were routinely checked by TLC using Merck Kieselgel 60 F_{254} aluminum plates and visualized by UV light. Regarding the reaction requiring the use of anhydrous solvents, the glassware was flame-dried and then cooled under a stream of dry argon before the use. Nuclear magnetic resonance spectra were recorded on a Varian Mercury 300 instrument (at 300 MHz) or on an Agilent Technologies 500 or 400 apparatus (at 500 or 400 MHz, respectively) at ambient temperature (25 °C at 300 MHz and 500 MHz; 27 °C at 400 MHz) in the specified deuterated solvent. Chemical shifts (δ) are quoted in parts per million (ppm) and are referenced to the residual solvent peak. The coupling constants *J* are given in Hertz (Hz). The following abbreviations were used: s (singlet), d (doublet), dd (doublet of doublets), t (triplet), dt (doublet of triplets), ddd (doublet of doublet of doublets), m (multiplet), br s (broad signal); signals due to OH and NH protons were located by deuterium exchange with D_2O. HRMS experiments were performed with a dual electrospray interface (ESI) and a quadrupole time-of-flight mass spectrometer (Q-TOF, Agilent 6530 Series Accurate-Mass Quadrupole Time-of-Flight LC/MS, Agilent Technologies Italia S.p.A., Cernusco sul Naviglio, Italy). Full-scan mass spectra were recorded in the mass/charge (*m/z*) range 50–3000 Da. Melting points for solid final compounds were determined by the capillary method on a Stuart Scientific SMP3 electrothermal apparatus and are uncorrected.

5.1.1. Synthesis of intermediates 2a-i

5.1.1.1. General procedure for the synthesis of amines 2a-c, 2i. Methyl-amine hydrochloride (9.0 mmol, 0.61 g) and potassium carbonate (4.5 mmol, 0.62 g) were suspended in anhydrous methanol (15 mL) in a flame-dried round-bottom flask and the reaction was stirred at room temperature for 30 min. The appropriate aldehyde (6.0 mmol) was added to the mixture and the reaction was kept under magnetic stirring at room temperature for 1 h. After cooling to 0 °C through an external ice bath, sodium borohydride (9.0 mmol, 0.34 g) was added portionwise

with caution. The reaction was stirred at 0 °C for 1 h and then warmed at room temperature for 2 h. Then ethyl acetate (6 mL) was added, and the solid residue was filtered off and washed with ethyl acetate. The solution was concentrated to dryness. The resulting crude was dissolved in ethyl acetate (50 mL) and washed with water (1 × 30 mL) followed by brine (1 × 30 mL). Then the organic layer was dried over anhydrous Na$_2$SO$_4$, filtered and the solvent was removed under rotatory evaporation. Free bases were transformed into the corresponding hydrochlorides **2a-c** by treatment with HCl 4.0 M in 1,4-dioxane. Compound **2i** was isolated after purification by flash chromatography (gradient elution: methanol in dichloromethane, 2% → 10%).

5.1.1.1.1. Synthesis of N-methyl(2-thienyl)methanaminium chloride (2a). Prepared from thiophene-2-carboxaldehyde (6.0 mmol, 0.67 g). Yield: 44%; white solid. ^{1}H NMR (300 MHz, DMSO-d_6) δ: 9.38 (s, 2H, dis. with D$_2$O), 7.61 (dd, J = 5.1, 1.0 Hz, 1H), 7.34–7.29 (m, 1H), 7.08 (dd, J = 5.1, 3.5 Hz, 1H), 4.30 (s, 2H), 2.47 (s, 3H, overlap with solvent residual peak).

5.1.1.1.2. Synthesis of 2-furyl-N-methylmethanaminium chloride (2b). Prepared from furan-2-carboxaldehyde (6.0 mmol, 0.58 g). Yield: 26%; brown solid. ^{1}H NMR (300 MHz, DMSO-d_6) δ: 9.34 (s, 2H, dis. with D$_2$O), 7.75 (s, 1H), 6.61 (d, J = 2.8 Hz, 1H), 6.53–6.48 (m, 1H), 4.15 (s, 2H), 2.46 (s, 3H, overlap with solvent residual peak).

5.1.1.1.3. Synthesis of N-methyl(3-thienyl)methanaminium chloride (2c). Prepared from thiophene-3-carboxaldehyde (6.0 mmol, 0.67 g). Yield: 43%; white solid. ^{1}H NMR (300 MHz, DMSO-d_6) δ: 9.10 (s, 2H, dis. with D$_2$O), 7.68–7.65 (m, 1H), 7.60 (dd, J = 4.9, 3.0 Hz, 1H), 7.26 (dt, J = 4.9, 1.6 Hz, 1H), 4.09 (s, 2H), 2.48 (s, 3H, overlap with solvent residual peak).

5.1.1.1.4. Synthesis of N-methyl-1-pyrimidin-5-ylmethanamine (2i). Prepared from pyrimidine-5-carboxaldehyde (6.0 mmol, 0.65 g). Yield: 48%; yellow oil. ^{1}H NMR (300 MHz, DMSO-d_6) δ: 9.04 (s, 1H), 8.71 (s, 2H), 3.63 (s, 2H), 2.24 (s, 3H), NH not detected.

5.1.1.2. Synthesis of (1H-imidazole-2-ylmethyl)methylamine (2d). 2-Imidazolecarboxaldehyde (2.5 mmol, 0.24 g) and methylamine (33 wt. % solution in absolute ethanol (7.5 mmol. 0.71 mL) were dissolved in anhydrous methanol (12 mL) and stirred at room temperature for 30 min. Sodium borohydride (3.8 mmol, 0.14 g) was added in portions without cooling. The reaction mixture was kept at room temperature for 16 h. Then the solvents were evaporated under reduced pressure and the resulting crude was suspended in dichloromethane (10 mL) and filtered. The filter cake was washed with dichloromethane and the solution was concentrated to dryness, thus furnishing the desired product that was used without further purification. Yield: 65%; brown oil. ^{1}H NMR (300 MHz, DMSO-d_6) δ: 6.87 (s, 2H), 3.62 (s, 2H), 2.24 (s, 3H), NHs not detected.

5.1.1.3. Synthesis of N-methyl-1-pyridin-4-ylmethanamine (2h) [41]. In a flame-dried two-neck round-bottom flask, pyridine-4-carboxaldehyde (2.5 mmol, 0.27 g) was dissolved in anhydrous methanol (2.5 mL). Then a solution of methylamine in absolute ethanol (33% w/w, 3.8 mmol, 0.36 mL) was added at room temperature. The reaction was refluxed for 2 h. After this period, the reaction was cooled to 0 °C using an external ice bath and sodium borohydride (1.8 mmol, 0.068 g) was added in small portions. The reaction mixture was left for additional 2 h at room temperature. Water was slowly added until gas evolution disappearance, then the mixture was concentrated under vacuum. The resulting residue was dissolved in dichloromethane (25 mL) and washed with brine (3 × 15 mL). The organic phase was dried over anhydrous Na$_2$SO$_4$, filtered, and concentrated to dryness. The residue was purified by column chromatography (gradient elution: methanol in dichloromethane, 5% → 10%). Yield: 62%; yellow oil. ^{1}H NMR (300 MHz, DMSO-d_6) δ: 8.47–8.44 (m, 2H), 7.32–7.29 (m, 2H), 3.64 (s, 2H), 2.23 (s, 3H), NH not detected.

5.1.1.4. General procedure for the synthesis of amines 2e-g. The appropriate aldehyde (2.3 mmol) was dissolved in anhydrous dichloromethane (15 mL) before adding a solution of methylamine in absolute ethanol (33 wt. %, 4.6 mmol, 0.43 mL). Then molecular sieves (4 Å) and anhydrous Na$_2$SO$_4$ (for **2e**: 0.57 mmol, 0.81 g) were added. The mixture was stirred at room temperature overnight. The inorganic residue was removed by filtration and the remaining solution was concentrated to dryness. The crude product was dissolved in absolute ethanol (15 mL) and sodium borohydride (3.5 mmol, 0.13 g) was added portionwise. The reaction mixture was left under magnetic stirring at room temperature (**2e**: overnight; **2f**: 5 h; **2g**: 3 h). Water was added to the mixture until effervescence disappeared. The solvent was evaporated under vacuum and the residue was suspended in brine (40 mL) and extracted with chloroform (3 × 20 mL). The collected organic layers were dried over anhydrous Na$_2$SO$_4$, filtered, and concentrated to dryness. The residue was purified by column chromatography (gradient eluent as indicated below) affording the desired product.

5.1.1.4.1. Synthesis of N-methyl-1-(1,3-thiazol-2-yl)methanamine (2e). Prepared from 1,3-thiazole-2-carbaldehyde (2.3 mmol, 0.26 g). Purification procedure: column chromatography (gradient elution: methanol in dichloromethane, 1% → 5%). Yield: 44%; brown oil. ^{1}H NMR (300 MHz, DMSO-d_6) δ: 7.68 (d, J = 3.2 Hz, 1H), 7.57 (d, J = 3.2 Hz, 1H), 3.91 (s, 2H), 2.32 (s, 3H), NH not detected.

5.1.1.4.2. Synthesis of N-methyl-1-(1,3-thiazol-4-yl)methanamine (2f). Prepared from 1,3-thiazole-4-carbaldehyde (2.3 mmol, 0.26 g). Purification procedure: flash chromatography (gradient elution: methanol in dichloromethane, 0% → 10%). Yield: 51%; brown oil. ^{1}H NMR (300 MHz, DMSO-d_6) δ: 9.04 (d, J = 1.9 Hz, 1H), 7.48 (d, J = 1.9 Hz, 1H), 3.82 (s, 2H), 2.31 (s, 3H), NH not detected.

5.1.1.4.3. Synthesis of N-methyl-1-(pyridin-3-yl)methanamine (2g). Prepared from 3-pyridinecarboxaldehyde (2.3 mmol, 0.22 mL). Purification procedure: column chromatography (gradient elution: methanol in dichloromethane, 5% → 15%). Yield: 62%; yellow oil. ^{1}H NMR (300 MHz, DMSO-d_6) δ: 8.48 (d, J = 1.7 Hz, 1H), 8.41 (dd, J = 4.8, 1.7 Hz, 1H), 7.69 (dt, J = 7.7, 1.7 Hz, 1H), 7.31 (ddd, J = 7.7, 4.8, 0.5 Hz, 1H), 3.63 (s, 2H), 2.23 (s, 3H), NH not detected.

5.1.2. Synthesis of intermediates 3a-b

5.1.2.1. General procedure for the synthesis of bromides 3a-b. In a round-bottom flask the appropriate alcohol (2.0 mmol) was dissolved in anhydrous dichloromethane (8 mL) and tetrabromomethane (2.4 mmol, 0.79 g) was added. Then a solution of PPh$_3$ (2.6 mmol, 0.68 g) in anhydrous dichloromethane (2 mL) was dropped while cooling to 0 °C through an external ice bath. After the addition, the mixture was slowly warmed at room temperature and stirred for additional 2 h. The crude product was concentrated under rotary evaporation and purified by flash chromatography (eluent: *n*-hexane).

5.1.2.1.1. Synthesis of 2-(2-bromoethyl)thiophene (3a). Prepared from 2-thiopheneethanol (2.0 mmol, 0.22 mL). Yield: quantitative yield; colorless oil. ^{1}H NMR (300 MHz, DMSO-d_6) δ: 7.38–7.35 (m, 1H), 6.98–6.96 (m, 1H), 6.96–6.94 (m, 1H), 3.69 (t, J = 7.0 Hz, 2H), 3.32 (t, J = 7.0 Hz, 2H).

5.1.2.1.2. Synthesis of 3-(2-bromoethyl)thiophene (3b). Prepared from 3-thiopheneethanol (2.0 mmol, 0.22 mL). Yield: 89%; colorless oil. ^{1}H NMR (300 MHz, DMSO-d_6) δ: 7.46 (dd, J = 4.9, 2.9 Hz, 1H), 7.29 (dd, J = 2.9, 1.3 Hz, 1H), 7.06 (dd, J = 4.9, 1.3 Hz, 1H), 3.70 (t, J = 7.3 Hz, 2H), 3.12 (t, J = 7.3 Hz, 2H).

5.1.3. Synthesis of final compounds 5–13, 16

5.1.3.1. General procedure for the synthesis of final compounds 5–13, 16. Appropriate ammine **2a-i** or commercially available *N*-methyl-2-(pyridin-3-yl)ethan-1-amine (1.2–2.0 eq) was suspended in anhydrous acetone or tetrahydrofuran (4.5 mL). Triethylamine (4.0 eq) or

potassium carbonate (4.8–8.0 eq) was added, followed by intermediate **4a** [18] (0.45 mmol, 0.17 g). After stirring at room temperature for 2–24 h, the reaction mixture was concentrated to dryness. The solid residue was suspended in chloroform, then the inorganic by-product was filtered off after several washing cycle with chloroform. The solvent was removed under rotatory evaporation, and the resulting crude was purified by chromatography (gradient elution, different mixture of methanol in dichloromethane as indicated below).

5.1.3.1.1. Synthesis of 4-(hydroxymethyl)-7-[(4-{[methyl(2-thienylmethyl)amino]methyl}benzyl)oxy]-2H-chromen-2-one (5). Prepared from **2a** (0.90 mmol, 0.15 g) and triethylamine (1.8 mmol, 0.25 mL) in anhydrous acetone overnight. Purification procedure: column chromatography (eluent: methanol in dichloromethane, 2%). Yield: 46%; m.p.: 63–6 °C; yellow solid. ^{1}H NMR (300 MHz, DMSO-d_6) δ: 7.60 (d, J = 8.8 Hz, 1H), 7.45–7.39 (m, 3H), 7.35 (d, J = 8.0 Hz, 2H), 7.07 (d, J = 2.4 Hz, 1H), 7.01–6.94 (m, 3H), 6.28 (s, 1H), 5.59 (t, J = 5.5 Hz, 1H, dis. with D$_2$O), 5.18 (s, 2H), 4.70 (dd, J = 5.5, 0.9 Hz, 2H), 3.70 (s, 2H), 3.50 (s, 2H), 2.12 (s, 3H). ^{13}C NMR (126 MHz, DMSO-d_6) δ: 161.68 (s), 160.88 (s), 157.11 (s), 155.14 (s), 143.00 (s), 139.24 (s), 135.34 (s), 129.12 (s), 128.33 (s), 126.99 (s), 126.21 (s), 125.86 (s), 125.78 (s), 113.11 (s), 111.27 (s), 107.94 (s), 102.19 (s), 70.16 (s), 60.39 (s), 59.52 (s), 55.76 (s), 41.97 (s). Anal. (C$_{24}$H$_{23}$NO$_4$S) calcd % C, 68.39; H, 5.50; N, 3.32; found % C, 68.86; H, 5.55; N, 3.13. HRMS (ESI) Calcd for (C$_{24}$H$_{23}$NO$_4$S): [M+Na]$^+$ *m/z:* 444.1240, found 444.1261; [M+H]$^+$ *m/z:* 422.1421, found 422.1426; [M − H]$^-$ *m/z:* 420.1275, found 420.1272.

5.1.3.1.2. Synthesis of 7-[(4-{[(2-furylmethyl)(methyl)amino]methyl}benzyl)oxy]-4-(hydroxymethyl)-2H-chromen-2-one (6). Prepared from **2b** (0.90 mmol, 0.13 g) and triethylamine (1.8 mmol, 0.25 mL) in anhydrous acetone overnight. Purification procedure: column chromatography (gradient elution: acetate in dichloromethane, 30% → 80%). Yield: 44%; m.p.: 93–5 °C; brown solid. ^{1}H NMR (300 MHz, DMSO-d_6) δ: 7.65–7.57 (m, 2H), 7.41 (d, J = 8.1 Hz, 2H), 7.32 (d, J = 8.1 Hz, 2H), 7.07 (d, J = 2.4 Hz, 1H), 6.99 (dd, J = 8.8, 2.4 Hz, 1H), 6.39 (dd, J = 3.1, 1.8 Hz, 1H), 6.31–6.25 (m, 2H), 5.60 (t, J = 5.4 Hz, 1H, dis. with D$_2$O), 5.18 (s, 2H), 4.70 (d, J = 5.4 Hz, 2H), 3.52 (s, 2H), 3.47 (s, 2H), 2.08 (s, 3H). ^{13}C NMR (126 MHz, DMSO-d_6) δ: 161.68 (s), 160.93 (s), 157.11 (s), 155.13 (s), 152.56 (s), 142.77 (s), 139.24 (s), 135.29 (s), 129.24 (s), 128.29 (s), 125.85 (s), 113.15 (s), 111.26 (s), 110.73 (s), 109.03 (s), 107.94 (s), 102.18 (s), 70.16 (s), 60.46 (s), 59.52 (s), 53.09 (s), 41.80 (s). Anal. (C$_{24}$H$_{23}$NO$_5$) calcd % C, 71.10; H, 5.72; N, 3.45; found % C, 70.79; H, 5.81; N, 3.12. HRMS (ESI) Calcd for (C$_{24}$H$_{23}$NO$_5$): [M+Na]$^+$ *m/z:* 428.1468, found 428.1469; [M − H]$^-$ *m/z:* 404.1503, found 404.1493.

5.1.3.1.3. Synthesis of 4-(hydroxymethyl)-7-[(4-{[methyl(3-thienylmethyl)amino]methyl}benzyl)oxy]-2H-chromen-2-one (7). Prepared from **2c** (0.90 mmol, 0.15 g) and triethylamine (1.8 mmol, 0.25 mL) in anhydrous acetone overnight. Purification procedure: flash chromatography (gradient elution: methanol in dichloromethane, 2% → 5%). Yield: 61%; m.p.: 113–6 °C; white solid. ^{1}H NMR (500 MHz, DMSO-d_6) δ: 7.60 (d, J = 8.8 Hz, 1H), 7.47 (dd, J = 4.9, 2.9 Hz, 1H), 7.41 (d, J = 8.1 Hz, 2H), 7.34 (d, J = 8.1 Hz, 2H), 7.33–7.31 (m, 1H), 7.09–7.05 (m, 2H), 6.98 (dd, J = 8.8, 2.5 Hz, 1H), 6.28 (t, J = 1.3 Hz, 1H), 5.59 (t, J = 5.5 Hz, 1H, dis. with D$_2$O), 5.18 (s, 2H), 4.71 (dd, J = 5.5, 1.3 Hz, 2H), 3.50 (s, 2H), 3.46 (s, 2H), 2.06 (s, 3H). ^{13}C NMR (126 MHz, DMSO-d_6) δ: 161.69 (s), 160.88 (s), 157.10 (s), 155.14 (s), 140.25 (s), 139.49 (s), 135.25 (s), 129.15 (s), 128.79 (s), 128.31 (s), 126.41 (s), 125.85 (s), 123.12 (s), 113.11 (s), 111.27 (s), 107.95 (s), 102.19 (s), 70.17 (s), 60.81 (s), 59.53 (s), 56.25 (s), 42.08 (s). Anal. (C$_{24}$H$_{23}$NO$_4$S) calcd % C, 68.39; H, 5.50; N, 3.32; found % C, 68.01; H, 5.63; N, 3.22. HRMS (ESI) Calcd for (C$_{24}$H$_{23}$NO$_4$S): [M+Na]$^+$ *m/z:* 444.1240, found 444.1241; [M+H]$^+$ *m/z:* 422.1421, found 422.1430; [M − H]$^-$ *m/z:* 420.1275, found 420.1263.

5.1.3.1.4. Synthesis of 4-(hydroxymethyl)-7-[(4-{[(1H-imidazole-2-ylmethyl)(methyl)amino]methyl}benzyl)oxy]-2H-chromen-2-one (8). Prepared from **2d** (0.54 mmol, 0.060 g) and potassium carbonate (1.1 mmol, 0.15 g) in anhydrous acetone for 3 h. Purification procedure: column chromatography (eluent: methanol in dichloromethane, 10%).

Yield: 27%; m.p.: 205–8 °C; white solid. ^{1}H NMR (500 MHz, DMSO-d_6) δ: 11.84 (br s, 1H, dis. with D$_2$O), 7.60 (d, J = 8.9 Hz, 1H), 7.40 (d, J = 8.2 Hz, 2H), 7.36 (d, J = 8.2 Hz, 2H), 7.07 (d, J = 2.5 Hz, 1H), 7.02 (br s, 1H), 6.98 (dd, J = 8.9, 2.5 Hz, 1H), 6.79 (br s, 1H), 6.28 (d, J = 1.3 Hz, 1H), 5.60 (t, J = 5.1 Hz, 1H, dis. with D$_2$O), 5.18 (s, 2H), 4.75–4.67 (m, 2H), 3.53 (s, 2H), 3.48 (s, 2H), 2.05 (s, 3H). ^{13}C NMR (126 MHz, DMSO-d_6) δ: 161.68 (s), 160.88 (s), 157.11 (s), 155.14 (s), 145.33 (s), 139.10 (s), 135.26 (s), 129.38 (s), 128.22 (s), 127.64 (s), 125.85 (s), 116.74 (s), 113.11 (s), 111.26 (s), 107.94 (s), 102.19 (s), 70.17 (s), 60.63 (s), 59.52 (s), 54.46 (s), 42.02 (s). Anal. (C$_{23}$H$_{23}$N$_3$O$_4$) calcd % C, 68.13; H, 5.72; N, 10.36; found % C, 68.54; H, 5.84; N, 10.15. HRMS (ESI) Calcd for (C$_{23}$H$_{23}$N$_3$O$_4$): [M+Na]$^+$ *m/z:* 428.1581, found 428.1574; [M − H]$^-$ *m/z:* 404.1616, found 404.1610.

5.1.3.1.5. Synthesis of 4-(hydroxymethyl)-7-[(4-{[methyl(1,3-thiazol-2-ylmethyl)amino]methyl}benzyl)oxy]-2H-chromen-2-one (9). Prepared from **2e** (0.54 mmol, 0.069 g) and potassium carbonate (1.1 mmol, 0.15 g) in anhydrous acetone for 3 h. Purification procedure: column chromatography (eluent: methanol in dichloromethane, 5%). Yield: 68%; m.p.: 148–150 °C; white solid. ^{1}H NMR (500 MHz, DMSO-d_6) δ: 7.70 (d, J = 3.3 Hz, 1H), 7.65 (d, J = 3.3 Hz, 1H), 7.60 (d, J = 8.9 Hz, 1H), 7.44 (d, J = 8.1 Hz, 2H), 7.38 (d, J = 8.1 Hz, 2H), 7.07 (d, J = 2.5 Hz, 1H), 6.99 (dd, J = 8.9, 2.5 Hz, 1H), 6.28 (s, 1H), 5.59 (t, J = 5.5 Hz, 1H, dis. with D$_2$O), 5.19 (s, 2H), 4.71 (dd, J = 5.5, 1.4 Hz, 2H), 3.85 (s, 2H), 3.59 (s, 2H), 2.21 (s, 3H). ^{13}C NMR (126 MHz, DMSO-d_6) δ: 170.85 (s), 161.67 (s), 160.88 (s), 157.10 (s), 155.14 (s), 142.61 (s), 138.85 (s), 135.53 (s), 129.17 (s), 128.37 (s), 125.86 (s), 120.82 (s), 113.10 (s), 111.28 (s), 107.96 (s), 102.20 (s), 70.14 (s), 60.85 (s), 59.53 (s), 58.26 (s), 42.44 (s). Anal. (C$_{23}$H$_{22}$N$_2$O$_4$S) calcd % C, 65.38; H, 5.25; N, 6.63; found % C, 65.01; H, 5.40; N, 6.42. HRMS (ESI) Calcd for (C$_{23}$H$_{22}$N$_2$O$_4$S): [M+Na]$^+$ *m/z:* 445.1192, found 445.1208; [M − H]$^-$ *m/z:* 421.1228, found 421.1228.

5.1.3.1.6. Synthesis of 4-(hydroxymethyl)-7-[(4-{[methyl(1,3-thiazol-4-ylmethyl)amino]methyl}benzyl)oxy]-2H-chromen-2-one (10). Prepared from **2f** (0.54 mmol, 0.069 g) and potassium carbonate (1.1 mmol, 0.15 g) in anhydrous acetone for 24 h. Purification procedure: flash chromatography (gradient elution: methanol in dichloromethane, 2% → 4%). Yield: 40%; m.p.: 133–6 °C; white solid. ^{1}H NMR (300 MHz, DMSO-d_6) δ: 9.04 (d, J = 1.8 Hz, 1H), 7.60 (d, J = 8.8 Hz, 1H), 7.52 (d, J = 1.8 Hz, 1H), 7.41 (d, J = 8.1 Hz, 2H), 7.36 (d, J = 8.1 Hz, 2H), 7.07 (d, J = 2.4 Hz, 1H), 6.98 (dd, J = 8.8, 2.4 Hz, 1H), 6.28 (s, 1H), 5.59 (t, J = 5.5 Hz, 1H, dis. with D$_2$O), 5.18 (s, 2H), 4.70 (dd, J = 5.5, 1.1 Hz, 2H), 3.69 (s, 2H), 3.53 (s, 2H), 2.12 (s, 3H). ^{13}C NMR (126 MHz, DMSO-d_6) δ: 161.68 (s), 160.94 (s), 157.11 (s), 155.12 (s), 154.98 (s), 153.98 (s), 139.39 (s), 135.24 (s), 129.24 (s), 128.28 (s), 125.85 (s), 116.91 (s), 113.15 (s), 111.26 (s), 107.93 (s), 102.18 (s), 70.16 (s), 60.79 (s), 59.52 (s), 56.49 (s), 42.11 (s). Anal. (C$_{23}$H$_{22}$N$_2$O$_4$S) calcd % C, 65.38; H, 5.25; N, 6.63; found % C, 65.56; H, 5.31; N, 6.45. HRMS (ESI) Calcd for (C$_{23}$H$_{22}$N$_2$O$_4$S): [M+Na]$^+$ *m/z:* 445.1192, found 445.1199; [M − H]$^-$ *m/z:* 421.1228, found 421.1225.

5.1.3.1.7. Synthesis of 4-(hydroxymethyl)-7-[(4-{[methyl(pyridin-3-ylmethyl)amino]methyl}benzyl)oxy]-2H-chromen-2-one (11). Prepared from **2g** (0.90 mmol, 0.11 g) and potassium carbonate (1.8 mmol, 0.25 g) in anhydrous acetone for 2 h. Purification procedure: column chromatography (eluent: methanol in dichloromethane, 5%). Yield: 71%; m.p.: 137–140 °C; white solid. ^{1}H NMR (500 MHz, DMSO-d_6) δ: 8.51 (d, J = 1.4 Hz, 1H), 8.45 (dd, J = 4.7, 1.4 Hz, 1H), 7.73 (dt, J = 7.8, 1.4 Hz, 1H), 7.60 (d, J = 8.8 Hz, 1H), 7.42 (d, J = 8.1 Hz, 2H), 7.36 (d, J = 8.1 Hz, 2H), 7.35–7.32 (m, 1H), 7.07 (d, J = 2.5 Hz, 1H), 6.98 (dd, J = 8.8, 2.5 Hz, 1H), 6.28 (t, J = 1.3 Hz, 1H), 5.59 (t, J = 5.5 Hz, 1H, dis. with D$_2$O), 5.19 (s, 2H), 4.71 (dd, J = 5.5, 1.3 Hz, 2H), 3.51 (s, 2H), 3.51 (s, 2H), 2.06 (s, 3H). ^{13}C NMR (126 MHz, DMSO-d_6) δ: 161.68 (s), 160.88 (s), 157.10 (s), 155.14 (s), 150.30 (s), 148.73 (s), 139.27 (s), 136.75 (s), 135.38 (s), 134.77 (s), 129.19 (s), 128.36 (s), 125.86 (s), 123.88 (s), 113.11 (s), 111.27 (s), 107.95 (s), 102.19 (s), 70.15 (s), 61.10 (s), 59.53 (s), 58.56 (s), 41.95 (s). Anal. (C$_{25}$H$_{24}$N$_2$O$_4$) calcd % C, 72.10; H, 5.81; N, 6.73; found % C, 72.01; H, 5.69; N, 6.58. HRMS (ESI) Calcd for

($C_{25}H_{24}N_2O_4$): [M+Na]$^+$ *m/z*: 439.1628, found 439.1619; [M − H]$^-$ *m/z*: 415.1663, found 415.1647.

5.1.3.1.8. Synthesis of 4-(hydroxymethyl)-7-[(4-{[methyl(pyridin-4-ylmethyl)amino]methyl}benzyl)oxy]-2H-chromen-2-one **(12)**. Prepared from **2h** (0.90 mmol, 0.11 g) and potassium carbonate (1.8 mmol, 0.25 g) in anhydrous acetone for 2 h. Purification procedure: column chromatography (eluent: methanol in dichloromethane, 5%). Yield: 67%: m. p.: 69–71 °C; white solid. ^{1}H NMR (500 MHz, DMSO-d_6) δ: 8.50 (d, *J* = 5.5 Hz, 2H), 7.60 (d, *J* = 8.8 Hz, 1H), 7.43 (d, *J* = 8.0 Hz, 2H), 7.38 (d, *J* = 8.0 Hz, 2H), 7.35 (d, *J* = 5.5 Hz, 2H), 7.07 (d, *J* = 2.4 Hz, 1H), 6.98 (dd, *J* = 8.8, 2.4 Hz, 1H), 6.28 (s, 1H), 5.59 (t, *J* = 5.4 Hz, 1H, dis. with D$_2$O), 5.18 (s, 2H), 4.71 (d, *J* = 5.4 Hz, 2H), 3.51 (s, 4H), 2.08 (s, 3H). ^{13}C NMR (126 MHz, DMSO-d_6) δ: 161.67 (s), 160.88 (s), 157.10 (s), 155.14 (s), 150.00 (s), 148.64 (s), 139.15 (s), 135.43 (s), 129.19 (s), 128.37 (s), 125.85 (s), 123.99 (s), 113.11 (s), 111.28 (s), 107.96 (s), 102.19 (s), 70.14 (s), 61.23 (s), 60.10 (s), 59.53 (s), 42.20 (s). Anal. ($C_{25}H_{24}N_2O_4$) calcd % C, 72.10; H, 5.81; N, 6.73; found % C, 72.41; H, 6.02; N, 6.44. HRMS (ESI) Calcd for ($C_{25}H_{24}N_2O_4$): [M+Na]$^+$ *m/z*: 439.1628, found 439.1635; [M+H]$^+$ *m/z*: 417.1809, found 417.1809; [M − H]$^-$ *m/z*: 415.1663, found 415.1650.

5.1.3.1.9. Synthesis of 4-(hydroxymethyl)-7-[(4-{[methyl(pyrimidin-5-ylmethyl)amino]methyl}benzyl)oxy]-2H-chromen-2-one **(13)**. Prepared from **2i** (0.90 mmol, 0.11 g) and potassium carbonate (1.8 mmol, 0.25 g) in anhydrous acetone for 2 h. Purification procedure: column chromatography (eluent: methanol in dichloromethane, 5%). Yield: 57%; m.p.: 129–131 °C; white solid. ^{1}H NMR (300 MHz, DMSO-d_6) δ: 9.07 (s, 1H), 8.74 (s, 2H), 7.60 (d, *J* = 8.9 Hz, 1H), 7.42 (d, *J* = 8.0 Hz, 2H), 7.36 (d, *J* = 8.0 Hz, 2H), 7.07 (d, *J* = 2.4 Hz, 1H), 6.98 (dd, *J* = 8.9, 2.4 Hz, 1H), 6.28 (s, 1H), 5.59 (t, *J* = 5.5 Hz, 1H, dis. with D$_2$O), 5.18 (s, 2H), 4.70 (d, *J* = 5.5 Hz, 2H), 3.55 (s, 2H), 3.53 (s, 2H), 2.07 (s, 3H). ^{13}C NMR (126 MHz, DMSO-d_6) δ: 161.67 (s), 160.88 (s), 157.78 (s), 157.57 (s), 157.09 (s), 155.14 (s), 139.01 (s), 135.45 (s), 132.67 (s), 129.23 (s), 128.37 (s), 125.85 (s), 113.11 (s), 111.27 (s), 107.96 (s), 102.19 (s), 70.14 (s), 61.11 (s), 59.53 (s), 56.02 (s), 41.87 (s). Anal. ($C_{24}H_{23}N_3O_4$) calcd % C, 69.05; H, 5.55; N, 10.07; found % C, 68.77; H, 5.52; N, 9.66. HRMS (ESI) Calcd for ($C_{24}H_{23}N_3O_4$): [M+Na]$^+$ *m/z*: 440.1581, found 440.1589; [M − H]$^-$ *m/z*: 416.1616, found 416.1613.

5.1.3.1.10. Synthesis of 4-(hydroxymethyl)-7-[(4-{[methyl(2-pyridin-3-ylethyl)amino]methyl}benzyl)oxy]-2H-chromen-2-one **(16)**. Prepared from commercially available *N*-methyl-2-(pyridin-3-yl)ethan-1-amine **2j** (0.90 mmol, 0.12 g) and potassium carbonate (1.8 mmol, 0.25 g) in anhydrous tetrahydrofuran for 3 h in the dark. Purification procedure: column chromatography (gradient elution: methanol in dichloromethane, 4% → 7%). Yield: 58%; m.p.: 145–7 °C; white solid. ^{1}H NMR (500 MHz, DMSO-d_6) δ: 8.41 (d, *J* = 1.8 Hz, 1H), 8.37 (dd, *J* = 4.8, 1.8 Hz, 1H), 7.60 (d, *J* = 8.8 Hz, 1H), 7.58 (dt, *J* = 7.8, 1.8 Hz, 1H), 7.36 (d, *J* = 8.0 Hz, 2H), 7.26 (ddd, *J* = 7.8, 4.8, 0.8 Hz, 1H), 7.21 (d, *J* = 8.0 Hz, 2H), 7.06 (d, *J* = 2.5 Hz, 1H), 6.98 (dd, *J* = 8.8, 2.5 Hz, 1H), 6.28 (t, *J* = 1.3 Hz, 1H), 5.59 (t, *J* = 5.5 Hz, 1H, dis. with D$_2$O), 5.17 (s, 2H), 4.70 (dd, *J* = 5.5, 1.3 Hz, 2H), 3.50 (s, 2H), 2.76 (t, *J* = 7.3 Hz, 2H), 2.57 (t, *J* = 7.3 Hz, 2H), 2.16 (s, 3H). ^{13}C NMR (126 MHz, DMSO-d_6) δ: 161.67 (s), 160.88 (s), 157.10 (s), 155.13 (s), 150.32 (s), 147.53 (s), 139.42 (s), 136.55 (s), 136.39 (s), 135.17 (s), 129.14 (s), 128.18 (s), 125.84 (s), 123.67 (s), 113.12 (s), 111.26 (s), 107.94 (s), 102.19 (s), 70.15 (s), 61.29 (s), 59.53 (s), 58.26 (s), 42.06 (s), 30.34 (s). Anal. ($C_{26}H_{26}N_2O_4$) calcd % C, 72.54; H, 6.09; N, 6.51; found % C, 72.88; H, 6.43; N, 6.84. HRMS (ESI) Calcd for ($C_{26}H_{26}N_2O_4$): [M+Na]$^+$ *m/z*: 453.1785, found 453.1788; [M − H]$^-$ *m/z*: 429.1820, found 429.1818.

5.1.4. Synthesis of final compounds **14–15**

*5.1.4.1. General procedure for the synthesis of final compounds **14–15***. Intermediate **4b** [18] (0.60 mmol, 0.20 g) was suspended in anhydrous acetonitrile (6 mL) before adding potassium carbonate (0.60 mmol, 0.082 g), potassium iodide in catalytic amount, and appropriate

bromide **3a-b** (0.40 mmol, 0.076 g). The reaction mixture was heated for 7 h at 70 °C. After cooling at room temperature, the solvent was removed under reduced pressure and the resulting crude was suspended in chloroform. The inorganic solid was filtered off after washing with chloroform. The solution was concentrated under rotary evaporation and the resulting solid was purified by flash chromatography (gradient elution: methanol in dichloromethane, 1% → 5%) to furnish the desired product.

5.1.4.1.1. Synthesis of 4-(hydroxymethyl)-7-{[4-({methyl[2-(2-thienyl)ethyl]amino}methyl)benzyl]oxy}-2H-chromen-2-one **(14)**. Prepared from **3a** (0.40 mmol, 0.076 g). Yield: 53%; m.p.: 106–8 °C; white solid. ^{1}H NMR (300 MHz, DMSO-d_6) δ: 7.63 (d, *J* = 8.8 Hz, 1H), 7.42 (d, *J* = 8.1 Hz, 2H), 7.33 (d, *J* = 8.1 Hz, 2H), 7.30 (dd, *J* = 5.1, 1.2 Hz, 1H), 7.09 (d, *J* = 2.5 Hz, 1H), 7.01 (dd, *J* = 8.8, 2.5 Hz, 1H), 6.93 (dd, *J* = 5.1, 3.4 Hz, 1H), 6.86 (dd, *J* = 3.4, 1.2 Hz, 1H), 6.31 (s, 1H), 5.62 (t, *J* = 5.5 Hz, 1H, dis. with D$_2$O), 5.21 (s, 2H), 4.73 (dd, *J* = 5.5, 1.4 Hz, 2H), 3.54 (s, 2H), 3.00 (t, *J* = 7.3 Hz, 2H), 2.62 (t, *J* = 7.3 Hz, 2H), 2.18 (s, 3H). ^{13}C NMR (101 MHz, DMSO-d_6) δ: 161.72 (s), 160.93 (s), 157.16 (s), 155.18 (s), 143.14 (s), 139.47 (s), 135.25 (s), 129.30 (s), 128.26 (s), 127.06 (s), 125.89 (s), 125.30 (s), 124.29 (s), 113.18 (s), 111.30 (s), 107.97 (s), 102.24 (s), 70.19 (s), 61.42 (s), 59.56 (s), 58.78 (s), 42.07 (s), 27.74 (s). Anal. ($C_{25}H_{25}NO_4S$) calcd % C, 68.94; H, 5.79; N, 3.22; found % C, 68.65; H, 5.90; N, 3.07. HRMS (ESI) Calcd for ($C_{25}H_{25}NO_4S$): [M+Na]$^+$ *m/z*: 458.1397, found 458.1406; [M − H]$^-$ *m/z*: 434.1432, found 434.1412.

5.1.4.1.2. Synthesis of 4-(hydroxymethyl)-7-{[4-({methyl[2-(3-thienyl)ethyl]amino}methyl)benzyl]oxy}-2H-chromen-2-one **(15)**. Prepared from **3b** (0.40 mmol, 0.076 g). Yield: 54%; m.p.: 140–3 °C; white solid. ^{1}H NMR (300 MHz, DMSO-d_6) δ: 7.61 (d, *J* = 8.9 Hz, 1H), 7.43–7.39 (m, 1H), 7.39 (d, *J* = 7.8 Hz, 2H), 7.28 (d, *J* = 7.8 Hz, 2H), 7.15 (d, *J* = 2.2 Hz, 1H), 7.07 (d, *J* = 2.4 Hz, 1H), 6.99 (dd, *J* = 8.9, 2.4 Hz, 1H), 6.97–6.94 (m, 1H), 6.29 (s, 1H), 5.60 (t, *J* = 5.6 Hz, 1H, dis. with D$_2$O), 5.18 (s, 2H), 4.71 (dd, *J* = 5.6, 1.2 Hz, 2H), 3.51 (s, 2H), 2.77 (t, *J* = 7.6 Hz, 2H), 2.57 (t, *J* = 7.6 Hz, 2H), 2.15 (s, 3H). ^{13}C NMR (101 MHz, DMSO-d_6) δ: 161.72 (s), 160.93 (s), 157.16 (s), 155.18 (s), 141.08 (s), 139.59 (s), 135.20 (s), 129.25 (s), 129.05 (s), 128.25 (s), 125.99 (s), 125.89 (s), 121.25 (s), 113.17 (s), 111.30 (s), 107.97 (s), 102.23 (s), 70.20 (s), 61.45 (s), 59.56 (s), 58.00 (s), 42.15 (s), 28.02 (s). Anal. ($C_{25}H_{25}NO_4S$) calcd % C, 68.94; H, 5.79; N, 3.22; found % C, 69.11; H, 5.60; N, 3.12. HRMS (ESI) Calcd for ($C_{25}H_{25}NO_4S$): [M+Na]$^+$ *m/z*: 458.1397, found 458.1386; [M − H]$^-$ *m/z*: 434.1432, found 434.1422.

5.2. Kinetic solubility and permeability (PAMPA-HDM)

Kinetic solubility measurement in phosphate buffered saline (PBS, pH = 7.4) was combined with a permeability assay (Parallel Artificial Membrane Permeation Assay; PAMPA) into a single workflow, where an aliquot of the filtrate from the Solubility filter plate was added to the donor compartment of the MultiScreen filter plate for PAMPA analysis. The kinetic aqueous solubility was estimated in duplicate by mixing, incubating (2 h with gentle shaking) and filtering a solution (1% DMSO) in a solubility polycarbonate filter plate. Solutions were filtered into a 96-well collection plate under vacuum and analyzed by UV–Vis spectroscopy. The relative solubility was then calculated using the sum of the recorded values as compared to a standard calibration curve. In PAMPA determination, the donor compartment was separate from an acceptor compartment by a hexadecane liquid layer on a polycarbonate membrane support. Analyses were carried out with a 96-well MultiScreen Permeability plate in duplicate by UV–Vis spectroscopy in PBS buffer at pH 7.4. Membrane retention was also evaluated. The obtained results were evaluated according to classification criteria which were recognized at TES Pharma on the basis of literature information and experimental results correlations [42]. Solubility classification ranges: S < 10 μM = low; 10 μM < S < 100 μM = moderate; S > 100 μM = high. PAMPA-HDM classification ranges: $\log P_a < -5$ cm/s = low; -5 cm/s < $\log P_a < -4.5$ cm/s = moderate; $\log P_a > -4.5$ cm/s = high. The table

below reports typical expected data for three control compounds.

cmpd	Solubility (μM, pH 7.4)	logP_a (cm/s)
testosterone	250	−3.9
diclofenac	>500	−4.8
furosemide	>500	< −6.5

The table below reports the data found in our experiments for three control compounds.

cmpd	Solubility (μM, pH 7.4)	logP_a (cm/s)
testosterone	265 ± 7	−3.8 ± 0.1
diclofenac	>500	−4.9 ± 0.1
furosemide	>500	< −6.5

5.3. Chromatographic hydrophobicity index (CHI)

In this chromatographic fast gradient reversed-phase method, the lipophilicity of compounds was assessed at three different pH values (2.0; 7.4; 10.5). The CHI value was obtained from the gradient (buffer/acetonitrile) retention time after calibrating the chromatographic system with a mixture of ten standard compounds. As detectors, both ion trap mass spectrometer and UV (240 nm) photomultiplier were used. The binary mobile phase was composed of acetonitrile and three different aqueous phases (trifluoroacetic acid 0.1% in water: pH 2.0; ammonium acetate 20 mM: pH 7.4 and 10.5) with different ratios according to the gradient method. CHI approximates the percentage (by volume) of acetonitrile required to achieve an equal distribution of compound between the mobile phase and the stationary phase of (C18 chromatographic column). The actual CHI value is calculated based on the calibration line of the reference compounds.

5.4. Microsomal stability

Test compounds were incubated (final concentration equal to 0.5 μM) with mouse microsomes supplemented with NADPH co-factors at 37 °C. Aliquots were taken at 6 time-points (0, 3, 6, 9, 15 and 30 min) in duplicates. At each time-point, the reactions were terminated by the addition of acetonitrile and mobile phase. The samples were centrifuged, and the parent compound concentration was evaluated by LC-MS/MS measurements. Dextromethorphan (Sigma-Aldrich) was used as standard [43]. Zero-time incubation was used as 100% value. The loss (as percentage) of substrate in incubation was determined to estimate in-vitro half-life and in-vitro intrinsic clearance of compounds. Half-life time of tested compound was calculated using the following equation (1):

$$t_{1/2} = \ln 2 \, / \, k \tag{1}$$

where k represents the kinetic constant of disappearance and is the slope of linear regression of logarithmic concentration of test item or controls vs. time.

The Intrinsic Clearance (CL$_{int}$) was calculated as follows:

$$CL_{int} \, (\mu L/min \times mg \, protein) = V \times 0.693 \, / \, t_{1/2} \tag{2}$$

where V is the incubation volume (μL)/microsomal protein (mg). Mouse intrinsic clearance classification ranges: CL$_{int}$ < 8.8 μL/min/mg = low; 8.8 μL/min/mg < CL$_{int}$ < 48 μL/min/mg = medium; CL$_{int}$ > 48 μL/min/mg = high. The assay is accepted when the control used in the assay (dextromethorphan) has clearance ≥10 μL/min/mg protein. In the assay conditions, dextromethorphan showed a half-life = 9.62 ± 0.62 min along with a CL$_{int}$ = 144.57 ± 9.22 μL/(min × mg) protein.

5.5. Cell-based studies

5.5.1. Materials

Dulbecco's modified Eagle's medium (DMEM), fetal bovine serum (FBS), penicillin and streptomycin (P/S) were purchased from GIBCO (Paisley, Scotland). Poly-lysine, trypsin, trypan blue, 3-(4,5-dimethylthiazol-2-yl)-2,5-diphenyltetrazolium bromide (MTT), and fluorescein isothiocyanate-dextran (FITC−D, average molecular weight 3000−5000) were purchased from Sigma (St. Louis, MO). Collagen I rat tail high concentration and transwell cell culture inserts were from Corning (New York). Human Neuroblastoma Cells (SH-SY5Y), astrocytes (DI-TNC1) and brain-immortalized endothelial cell line (bEnd3) were from American Type Culture Collection (ATCC). Hydrogen peroxide solution 30% stabilized and 6-hydroxydopamine (6-OHDA) were purchased from Sigma-Aldrich. All aqueous solutions were prepared by using water obtained from a Milli-Q gradient A-10 system (Millipore, 18.2 MΩ cm, organic carbon content ≥4 μg/L).

5.5.2. Cell viability and neuroprotection studies

5.5.2.1. Cell viability and neuroprotection in neuroblastoma cell line.
Human neuroblastoma SH-SY5Y cell line was cultured in Dulbecco's modified Eagle's medium (DMEM) high-glucose supplemented with 10% (v/v) heat-inactivated fetal bovine serum (FBS), 2 mM L-glutamine, 100 U/mL penicillin and 100 μg/mL streptomycin at 37 °C in an atmosphere of 5% CO$_2$. After reaching the confluence, cells were counted and plated in a 96-well plate at the concentration of 4.5×10^4 cell/well to assess the biocompatibility of compounds **7**, **15**, and **16** (tested at concentration from 1 to 100 μM) in DMEM serum-free for 24 h at 37 °C, 5% CO$_2$. The cell viability was evaluated by MTT [3-(4,5-dimethylthiazol-2-yl)-2,5-diphenyl tetrazolium bromide] assay [18] and results were expressed as percentage referred to untreated cells (CTRL). Triplicate cultures were set up for each concentration and experiments were performed for three times.

Compounds **7**, **15**, and **16** (0.1, 1, and 5 μM) were co-incubated with a non-specific oxidative insult (H$_2$O$_2$, 300 μM) for 24 h in DMEM-serum free at 37 °C, 5% CO$_2$, and then cell viability was determined by MTT assay. Controls were represented by untreated cells and by cells treated with H$_2$O$_2$ alone or with the antioxidant quercetin (QRC, 30 μM, as positive antioxidant control). Results were expressed as percentage of viable cells compared to untreated cells.

The potential neuroprotective effect of **7**, **15**, and **16** (0.1–5 μM) was also tested in the presence of a specific neurotoxic insult (6-hydroxydopamine, 6-OHDA, 200 μM) in DMEM-serum free for 24 h, at 37 °C, 5% CO$_2$. After treatment, the medium was removed and the neuroprotective effect was evaluated as cell viability gain (compared to insulted cells without compound) through the MTT assay. Controls were represented by untreated cells (negative control) or by cells treated with 6-OHDA with or without donepezil (0.1–5 μM, positive control). For these assays, three independent experiments with replicates were carried out and the results were expressed as percentage of viable cells compared to untreated cells.

5.5.2.2. Cell viability in bEnd3 and DI-TNC1 cell lines.
Brain immortalized mouse endothelial cell line (bEnd3) and astrocyte cell line (DI-TNC1) were grown at 37 °C, 5% CO$_2$ in DMEM high-glucose supplemented with 10% FBS, 100 U/mL penicillin, and 100 μg/mL streptomycin and maintained in T-75 flasks until the confluence. Then, cells were detached with trypsin 0.25%, centrifuged at 1500 rpm for 10 min, plated in a 96 well plate at the concentration of 4.5×10^4 cell/well and incubated at 37 °C, 5% CO$_2$. After 24 h, cells were treated with compounds **7** or **15** (1–100 μM) in DMEM serum-free for 24 h at 37 °C, 5% CO$_2$ to evaluate the potential cytotoxicity. The viability was determined by MTT test and the results were expressed as percentage referred to untreated cells. The experiments were performed in triplicates.

5.5.3. In vitro blood−brain barrier (BBB) model and permeability assay

The in vitro model of blood-brain barrier (BBB) was set up by co-culturing mouse bEnd3 cells and immortalized DI-TNC1 astrocytes (Fig. S20 in Supplementary Material) on inserts with a diameter of 10.5 mm containing a track-etched poly(ethylene terephthalate) (PET) membrane (0.4 µm pores). Briefly, the abluminal side and luminal side of the insert membrane were coated with poly-L-lysine (PLL) 0.01% and collagen Type I from rat tail (500 µg/mL) for 2 h, respectively. DI-TNC1 astrocytes and bEnd3 were grown in DMEM high glucose supplemented with 10 % FBS, 100 U/mL penicillin, and 100 µg/mL streptomycin, at 37 °C in 5% CO_2. Specifically, DI-TNC1 were plated at a density of 2.5×10^4 cells/cm^2 on the abluminal side using the insert flipped back. After 2 h of adhesion, the insert was flipped again and bEnd3 were plated on the luminal side at a density of 2×10^4 cells/cm^2. The control insert, represented by PLL- and collagen-coated insert without cells and inserts containing monoculture of DI-TNC1 or bEnd3, as well as the co-cultures of DI-TNC1/bEnd3 were placed in a 12-well plate in DMEM high glucose, 10 % FBS, 100 U/mL penicillin, 100 µg/mL streptomycin, and incubated at 37 °C, 5 % CO_2 until reaching the 80–90 % confluence. Starting from 3 days after plating, the medium was refreshed and measurements of transendothelial electrical resistance (TEER) were carried out using an epithelial voltmeter (Millicell® ERS-2) balanced for 30 min in ethanol and then in DMEM. The average TEER value of the control insert was subtracted from the average value of inserts containing the co-cultures or the monocultures of DI-TNC1 astrocytes and bEnd3 cells. TEER measurements were performed for three independent times on each sample and values were expressed as $\Omega \times cm^2 \pm SD$. From day 4, when the TEER value of the co-culture reached the maximum (Fig. S21 in Supplementary Material), the paracellular permeability of BBB was detected using fluorescein isothiocyanate−dextran (FITC−D) (MW 3000–5000). For this analysis, FITC−D was introduced into the upper chamber of the insert at the concentration of 200 µg/mL. After 2 h of incubation at 37 °C with 5 % CO_2, supernatants were collected from the upper and lower compartments and the fluorescence intensity was measured ($\lambda_{exc} = 485$ nm, $\lambda_{em} = 535$ nm). The control was represented by inserts coated with PLL and collagen Type I without cells. The amount of FITC−D permeated was determined by a calibration curve obtained with FITC−D solutions at known concentrations. The apparent permeability (P_a cm/s) was calculated according to the equation reported in Ref. [44] which takes into account the area of insert (cm), the time of permeation (sec), and the amount in the top and bottom vessel.

After the setup and validation of the BBB model, derivative **7** and **15** (20 µM) were added in the upper chamber of the inserts containing the cell co-cultures and incubated for 2 h at 37 °C in 5% CO_2. The controls were represented by inserts with co-cultures incubated with FITC-D and inserts with co-cultures incubated in the presence of donepezil (20 µM), a CNS-permeant anti-Alzheimer drug. Calibration curves were obtained in PBS by fluorescence measurements ($\lambda_{exc} = 320$ nm; $\lambda_{em} = 400$ nm) and the apparent permeability (P_a, cm/sec) was calculated as reported above. The experiments were run in triplicates and the P_a values were reported as the mean ± SD.

5.5.4. Statistical analysis

Data analysis was carried out by using GraphPad Prism 5.0 (Graph-Pad Software Inc., San Diego, CA, USA). Data were expressed as mean values ± SD compared to control (untreated cells) from three independent experiments, each performed in triplicates. Statistical analysis was performed by using one-way analysis of variance (ANOVA) followed by Dunnett's multiple comparison post hoc test for multiple comparison analysis. For cell viability determination, the levels of significance were referred to untreated cells (control). In cytoprotection experiments, the levels of significance were reported as follows: i) for cells incubated with insult alone (6-OHDA or H_2O_2, without compound under study), levels are referred to untreated cells (control: without compound, without insult); ii) for cells incubated with both insult and compound under study (compound + 6-OHDA or compound + H_2O_2), levels were referred

to treated cells with 6-OHDA or H_2O_2 alone (without compound under study).

5.6. Computational studies

5.6.1. Molecular docking simulations

Derivative **7** and **15** were docked on the published X-ray structures of *i) mus musculus* AChE (*m*AChE) in complex with 4-(hydroxymethyl)-7-[[4-[[methyl(phenylmethyl)amino]methyl]phenyl]methoxy]chromen-2-one (resolution 2.60 Å, pdb code: 7QAK [23]) and *ii) human* BChE (*h*BChE) in complex with (2-((1-(benzenesulfonyl)-1H-indol-4-yl)oxy) ethyl)(benzyl)amine (resolution 2.00 Å, pdb code: 7AWG [38]). The retrieved files were prepared using the Protein Preparation Workflow tool from the Schrodinger Suite 2022−4 [45]. Missing hydrogen atoms were added, incomplete side chains were reconstructed, and appropriate protonation states were assigned based on physiological pH. Non-essential water molecules were removed, and the hydrogen bonding network was optimized. Finally, the 3D protein structures underwent force field-based minimization using OPLS-4 [46]. Both ligands were processed using LigPrep [47], a tool from the Schrodinger Suite 2022−4, to remove salts and generate all possible tautomers and ionization states at a pH range of 7.0 ± 2.0. The prepared protein and ligand structures were used for docking simulations employing a grid-based approach with the GLIDE software [48]. Specifically, due to the lower similarity between our compounds and the cognate ligand, for simulations involving BChE, we used Induced Fit Docking (IFD) simulations to accommodate potential protein conformational changes during ligand binding. Docking simulations were conducted using the Standard Precision (SP) protocol with all default settings, utilizing a cubic grid centered on the co-crystallized ligand position. The grid dimensions comprised an inner box of 10 Å × 10 Å x 10 Å for all considered protein structures, and an outer box of 30 Å × 30 Å x 30 Å (25 Å × 25 Å x 25 Å) for 7QAK (7AWG). Regarding BChE, **7** and **15** share high similarity with the cognate ligand. Therefore, docking simulations were performed by constraining the exploration of conformational space, generating only those poses consistent with the crystallographic coordinates of the shared substructure with a tolerance of 1.5 Å.

5.6.2. Model system preparation and molecular dynamics simulation protocol

To investigate potential ligand-induced conformational changes in the binding site, we simulated the top-scored docking poses of four complexes (*h*BChE-**7**, *h*BChE-**15**, *m*AChE-**7**, *m*AChE-**15**) using MD simulations. Each complex was solvated with a minimized orthorhombic TIP3P [49] water box using the Desmond system builder tool [50]. This tool automatically calculated the simulation box size with a 10 Å buffer distance between the solutes and the box boundary, ensuring proper containment and preventing interaction with the box. Neutralizing Na^+ and Cl^- ions were added to achieve a 150 mM salt concentration, resulting in systems of approximately 50,000 atoms. The OPLS4 force field [46] was employed for both proteins and ligands. Simulations were conducted on GPUs using Desmond 4.2, integrated into the Schrödinger Suite 2022-4 [50], as software platform. A non-bonded cutoff of 9 Å was implemented. All prepared systems underwent minimization, equilibration, and production simulation using an isothermal-isobaric ensemble (NPT, P = 1 atm, T = 310 K) with a Nosè–Hoover thermostat [51] and a Martyna-Tobias-Klein barostat [52]. Each complex was subjected to a 150 ns-long MD simulation with a 2 fs time step, and coordinates were recorded at 50 ps intervals, generating 3000 frames for analysis per system. Trajectory analysis was performed using the trajectory player and simulation interaction diagram tools available in Schrödinger Suite 2022-4.

5.7. In vitro enzymatic inhibition assays

All human enzymes, substrates and reagents were from Sigma-

Aldrich (Milan, Italy). Experiments were run in 96-well plates from Greiner Bio-One (Kremsmenster, Austria) with an Infinite M1000 Pro multiplate reader (Tecan, Cernusco sul Naviglio, Italy). The inhibition of ChEs was determined by following Ellman's spectrophotometric assay [53] in transparent, flat-bottom plates [27]. For studies addressing MAOs inhibition the spectrofluorimetric protocol [26] was based on the oxidative deamination of kynuramine to 4-hydroxyquinoline measured in black, flat-bottom polystyrene plates. Incubations were performed in triplicate and results were expressed as the mean $\pm$ SEM from 3 independent experiments. The values of IC_{50} were calculated by nonlinear regressions using GraphPad Prism 5.00 (GraphPad Software, San Diego, CA, USA).

CRediT authorship contribution statement

Gabriella La Spada: Writing – original draft, Methodology. **Daniela Valeria Miniero:** Writing – original draft, Methodology. **Mariagrazia Rullo:** Writing – original draft, Methodology, Investigation. **Marco Cipolloni:** Writing – review & editing, Methodology. **Pietro Delre:** Writing – original draft, Methodology. **Carolina Colliva:** Writing – review & editing, Methodology. **Marco Colella:** Writing – original draft, Methodology. **Francesco Leonetti:** Writing – review & editing, Funding acquisition. **Grazia Maria Liuzzi:** Writing – review & editing, Supervision, Conceptualization. **Giuseppe Felice Mangiatordi:** Writing – review & editing, Supervision, Methodology, Conceptualization. **Nicola Giacchè:** Writing – review & editing, Supervision, Methodology, Data curation, Conceptualization. **Leonardo Pisani:** Writing – review & editing, Writing – original draft, Supervision, Methodology, Investigation, Funding acquisition, Conceptualization.

Declaration of competing interest

The authors declare that they have no known competing financial interests or personal relationships that could have appeared to influence the work reported in this paper.

Data availability

Data will be made available on request.

Appendix A. Supplementary data

Supplementary data to this article can be found online at https://doi.org/10.1016/j.ejmech.2024.116511.

References

[1] S. Saez-Atienzar, E. Masliah, Cellular senescence and Alzheimer disease: the egg and the chicken scenario, Nat. Rev. Neurosci. 21 (2020) 433–444.
[2] B. Winblad, P. Amouyel, S. Andrieu, C. Ballard, C. Brayne, H. Brodaty, A. Cedazo-Minguez, B. Dubois, D. Edvardsson, H. Feldman, L. Fratiglioni, G.B. Frisoni, S. Gauthier, J. Georges, C. Graff, K. Iqbal, F. Jessen, G. Johansson, L. Jönsson, M. Kivipelto, M. Knapp, F. Mangialasche, R. Melis, A. Nordberg, M.O. Rikkert, C. Qiu, T.P. Sakmar, P. Scheltens, L.S. Schneider, R. Sperling, L.O. Tjernberg, G. Waldemar, A. Wimo, H. Zetterberg, Defeating Alzheimer's disease and other dementias: a priority for European science and society, Lancet, Neurol. 15 (2016) 455–532.
[3] W.M. van der Flier, M.E. de Vugt, E.M.A. Smets, M. Blom, C.E. Teunissen, Towards a future where Alzheimer's disease pathology is stopped before the onset of dementia, Nat. Aging 3 (2023) 494–505.
[4] J.M. Long, D.M. Holtzman, Alzheimer disease: an update on pathobiology and treatment strategies, Cell 179 (2019) 312–339.
[5] H. Wang, H. Zhang, Reconsideration of anticholinesterase therapeutic strategies against Alzheimer's disease, ACS Chem. Neurosci. 10 (2019) 852–862.
[6] J.A. Hardy, G.A. Higgins, Alzheimer's disease: the amyloid cascade hypothesis, Science 256 (1992) 184–185.
[7] K. Herrup, The case for rejecting the amyloid cascade hypothesis, Nat. Neurosci. 18 (2015) 794–799.
[8] S. Reardon, FDA approves Alzheimer's drug lecanemab amid safety concerns, Nature 613 (2023) 227–228.
[9] M.L. Bolognesi, Harnessing polypharmacology with medicinal chemistry, ACS Med. Chem. Lett. 10 (2019) 273–275.
[10] M. Rullo, M. Catto, A. Carrieri, M. de Candia, C.D. Altomare, L. Pisani, Chasing ChEs-MAO B multi-targeting 4-aminomethyl-7-benzyloxy-2*H*-Chromen-2-ones, Molecules 24 (2019) 4507.
[11] L. Pisani, M. Catto, F. Leonetti, O. Nicolotti, A. Stefanachi, F. Campagna, A. Carotti, Targeting monoamine oxidases with multipotent ligands: an emerging strategy in the search of new drugs against neurodegenerative diseases, Curr. Med. Chem. 18 (2011) 4568–4587.
[12] F.J. Pérez-Areales, A.L. Turcu, M. Barniol-Xicota, C. Pont, D. Pivetta, A. Espargaró, M. Bartolini, A. De Simone, B. Andrisano, B. Pérez, R. Sabate, F.X. Sureda, S. Vázquez, D. Muñoz-Torrero, A novel class of multitarget anti-Alzheimer benzohomoadamantane−chlorotacrine hybrids modulating cholinesterases and glutamate NMDA receptors, Eur. J. Med. Chem. 180 (2019) 613–626.
[13] J. Reis, F. Cagide, M.E. Valencia, J. Teixeira, D. Bagetta, C. Pérez, E. Uriarte, P.J. Oliveira, F. Ortuso, S. Alcaro, M.I. Rodríguez-Franco, F. Borges, Multi-target-directed ligands for Alzheimer's disease: discovery of chromone-based monoamine oxidase/cholinesterase inhibitors, Eur. J. Med. Chem. 158 (2018) 781–800.
[14] N.H. Greig, T. Utsuki, D.K. Ingram, Y. Wang, G. Pepeu, C. Scali, Q.-S. Yu, J. Mamczarz, H.W. Holloway, T. Giordano, D. Chen, K. Furukawa, K. Sambamurti, A. Brossi, D.K. Lahiri, Selective butyrylcholinesterase inhibition elevates brain acetylcholine, augments learning and lowers Alzheimer beta-amyloid peptide in rodent, Proc. Natl. Acad. Sci. U.S.A. 102 (2005) 17213–17218.
[15] S. Darvesh, M.K. Cash, G.A. Reid, E. Martin, A. Mitnitski, C. Geula, Butyrylcholinesterase is associated with β-amyloid plaques in the transgenic APPSWE/PSEN1dE9 mouse model of Alzheimer disease, J. Neuropathol. Exp. Neurol. 71 (2012) 2–14.
[16] M.K. Cash, K. Rockwood, J.D. Fisk, S. Darvesh, Clinicopathological correlations and cholinesterase expression in early-onset familial Alzheimer's disease with the presenilin 1 mutation, Leu235Pro, Neurobiol. Aging 103 (2021) 31–41.
[17] S. Darvesh, Butyrylcholinesterase as a diagnostic and therapeutic target for Alzheimer's disease, Curr. Alzheimer Res. 13 (2016) 1173–1177.
[18] M. Rullo, M. Cipolloni, M. Catto, C. Colliva, D.V. Miniero, T. Latronico, M. de Candia, T. Benicchi, A. Linusson, N. Giacchè, C.D. Altomare, L. Pisani, Probing fluorinated motifs onto dual AChE-MAO B inhibitors: rational design, synthesis, biological evaluation, and early-ADME studies, J. Med. Chem. 65 (2022) 3962–3977.
[19] R. Sánchez-Rodríguez, F. Munari, R. Angioni, F. Venegas, A. Agnellini, M.P. Castro-Gil, A. Castegna, R. Luisetto, A. Viola, M. Canton, Targeting monoamine oxidase to dampen NLRP3 inflammasome activation in inflammation, Cell. Mol. Immunol. 18 (2021) 1311–1313.
[20] F. Leng, P. Edison, Neuroinflammation and microglial activation in Alzheimer disease: where do we go from here? Nat. Rev. Neurol. 17 (2021) 157–172.
[21] S.F. Carter, K. Herholz, P. Rosa-Neto, L. Pellerin, A. Nordberg, E.R. Zimmer, Astrocyte biomarkers in Alzheimer's disease, Trends Mol. Med. 25 (2019) 77–95.
[22] M.B.H. Youdim, D. Edmondson, K.F. Tipton, The therapeutic potential of monoamine oxidase inhibitors, Nat. Rev. Neurosci. 7 (2006) 295–309.
[23] F. Ekström, A. Gottinger, N. Forsgren, M. Catto, L.G. Iacovino, L. Pisani, C. Binda, Dual reversible coumarin inhibitors mutually bound to monoamine oxidase B and acetylcholinesterase crystal structures, ACS Med. Chem. Lett. 13 (2022) 499–506.
[24] R. Farina, L. Pisani, M. Catto, O. Nicolotti, D. Gadaleta, N. Denora, R. Soto-Otero, E. Mendez-Alvarez, C.S. Passos, G. Muncipinto, C.D. Altomare, A. Nurisso, P.-A. Carrupt, A. Carotti, Structure-based design and optimization of multitarget-directed 2 H -Chromen-2-one derivatives as potent inhibitors of monoamine oxidase B and cholinesterases, J. Med. Chem. 58 (2015) 5561–5578.
[25] M.A.M. Subbaiah, N.A. Meanwell, Bioisosteres of the phenyl ring: recent strategic applications in lead optimization and drug design, J. Med. Chem. 64 (2021) 14046–14128.
[26] M. Rullo, G. La Spada, D.V. Miniero, A. Gottinger, M. Catto, P. Delre, M. Mastromarino, T. Latronico, S. Marchese, G.F. Mangiatordi, C. Binda, A. Linusson, G.M. Liuzzi, L. Pisani, Bioisosteric replacement based on 1,2,4-oxa-diazoles in the discovery of 1H-indazole-bearing neuroprotective MAO B inhibitors, Eur. J. Med. Chem. 255 (2023) 115352.
[27] L. Pisani, M. Catto, A. De Palma, R. Farina, S. Cellamare, C.D. Altomare, Discovery of potent dual binding site acetylcholinesterase inhibitors via homo- and heterodimerization of coumarin-based moieties, ChemMedChem 12 (2017) 1349–1358.
[28] J.C. Shelley, A. Cholleti, L.L. Frye, J.R. Greenwood, M.R. Timlin, M. Uchimaya, Epik: a software program for pK a prediction and protonation state generation for drug-like molecules, J. Comput. Aided Mol. Des. 21 (2007) 681–691.
[29] R.C. Johnston, K. Yao, Z. Kaplan, M. Chelliah, K. Leswing, S. Seekins, S. Watts, D. Calkins, J. Chief Elk, S.V. Jerome, M.P. Repasky, J.C. Shelley, Epik: pKa and protonation state prediction through machine learning, J. Chem. Theor. Comput. 19 (2023) 2380–2388.

[30] K. Valkó, C. Bevan, D. Reynolds, Chromatographic hydrophobicity index by fast-gradient RP-HPLC: a high-throughput alternative to log P/log D, Anal. Chem. 69 (1997) 2022–2029.

[31] M. Ishikawa, Y. Hashimoto, Improvement in aqueous solubility in small molecule drug discovery programs by disruption of molecular planarity and symmetry, J. Med. Chem. 54 (2011) 1539–1554.

[32] D.F. Veber, S.R. Johnson, H.-Y. Cheng, B.R. Smith, K.W. Ward, K.D. Kopple, Molecular properties that influence the oral bioavailability of drug candidates, J. Med. Chem. 45 (2002) 2615–2623.

[33] S. Cetin, D. Knez, S. Gobec, J. Kos, A. Pišlar, Cell models for Alzheimer's and Parkinson's disease: at the interface of biology and drug discovery, Biomed. Pharmacother. 149 (2022) 112924.

[34] K. Hanrott, L. Gudmunsen, M.J. O'Neill, S. Wonnacott, 6-hydroxydopamine-induced apoptosis is mediated via extracellular auto-oxidation and caspase 3-dependent activation of protein kinase Cdelta, J. Biol. Chem. 281 (2006) 5373–5382.

[35] K.B. Magalingam, S.D. Somanath, P. Ramdas, N. Haleagrahara, A. K. Radhakrishnan, 6-Hydroxydopamine induces neurodegeneration in terminally differentiated SH-SY5Y neuroblastoma cells via enrichment of the nucleosomal degradation pathway: a global proteomics approach, J. Mol. Neurosci. 72 (2022) 1026–1046.

[36] B. Ossola, T.M. Kääräinen, A. Raasmaja, P.T. Männistö, Time-dependent protective and harmful effects of quercetin on 6-OHDA-induced toxicity in neuronal SH-SY5Y cells, Toxicology 250 (2008) 1–8.

[37] N. Rahemtulla, C.F. Deschepper, J. Maurice, B. Mittal, S. David, Immunocytochemical and functional characterization of an immortalized type 1 astrocytic cell line, Brain Res. 642 (1994) 221–227.

[38] T. Wichur, J. Godyń, I. Góral, G. Latacz, A. Bucki, A. Siwek, M. Głuch-Lutwin, B. Mordyl, J. Śniecikowska, M. Walczak, D. Knez, M. Jukič, K. Sałat, S. Gobec, M. Kołaczkowski, B. Malawska, X. Brazzolotto, A. Więckowska, Development and crystallography-aided SAR studies of multifunctional BuChE inhibitors and 5-HT6R antagonists with β-amyloid anti-aggregation properties, Eur. J. Med. Chem. 225 (2021) 113792.

[39] I.R. Macdonald, E. Martin, T.L. Rosenberry, S. Darvesh, Probing the peripheral site of human butyrylcholinesterase, Biochemistry 51 (2012) 7046–7053.

[40] J. Kua, Y. Zhang, A.C. Eslami, J.R. Butler, J.A. McCammon, Studying the roles of W86, E202, and Y337 in binding of acetylcholine to acetylcholinesterase using a combined molecular dynamics and multiple docking approach, Protein Sci. 12 (2003) 2675–2684.

[41] S. Chen, L. Yang, Y. Shang, J. Mao, P.J. Walsh, Base-promoted tandem synthesis of 2-azaaryl tetrahydroquinolines, Org. Lett. 23 (2021) 1594–1599.

[42] E.H. Kerns, L. Di, Drug-like Properties: Concepts, Structure Design and Methods: from ADME to Toxicity Optimization, 2008.

[43] J.D. Lutz, N. Isoherranen, Prediction of relative in vivo metabolite exposure from in vitro data using two model drugs: dextromethorphan and omeprazole, Drug Metab. Dispos. 40 (2012) 159–168.

[44] T. Latronico, F. Rizzi, A. Panniello, V. Laquintana, I. Arduino, N. Denora, E. Fanizza, S. Milella, C.M. Mastroianni, M. Striccoli, M.L. Curri, G.M. Liuzzi, N. Depalo, Luminescent PLGA nanoparticles for delivery of darunavir to the brain and inhibition of matrix metalloproteinase-9, a relevant therapeutic target of HIV-associated neurological disorders, ACS Chem. Neurosci. 12 (2021) 4286–4301.

[45] Schrödinger Release 2022-4: Protein Preparation Wizard; Epik, Schrödinger, LLC, New York, NY, 2024; Impact, Schrödinger, LLC, Schrödinger, LLC, New York, NY, 2022. New York, NY; Prime.

[46] C. Lu, C. Wu, D. Ghoreishi, W. Chen, L. Wang, W. Damm, G.A. Ross, M.K. Dahlgren, E. Russell, C.D. Von Bargen, R. Abel, R.A. Friesner, E.D. Harder, OPLS4: improving force field accuracy on challenging regimes of chemical space, J. Chem. Theor. Comput. 17 (2021) 4291–4300.

[47] Schrödinger Release 2022-4, LigPrep, Schrödinger, LLC, New York, NY, 2022.

[48] Schrödinger Release 2022-4: Glide, Schrödinger, LLC, New York, NY, 2022.

[49] P. Mark, L. Nilsson, Structure and dynamics of the TIP3P, SPC, and SPC/E water models at 298 K, J. Phys. Chem. A 105 (2001) 9954–9960.

[50] Schrödinger Release 2022-4: Desmond Molecular Dynamics System, D. E. Shaw Research, New York, NY, 2024, Maestro-Desmond Interoperability Tools, Schrödinger, New York, NY, 2022.

[51] D.J. Evans, B.L. Holian, The Nose–Hoover thermostat, J. Chem. Phys. 83 (1985) 4069–4074.

[52] G.J. Martyna, D.J. Tobias, M.L. Klein, Constant pressure molecular dynamics algorithms, J. Chem. Phys. 101 (1994) 4177–4189.

[53] G.L. Ellman, K.D. Courtney, V. Andres, R.M. Feather-Stone, A new and rapid colorimetric determination of acetylcholinesterase activity, Biochem. Pharmacol. 7 (1961) 88–95.